


Leveraging Small-Scale Quantum Computers with Unitarily Downfolded Hamiltonians

Renke Huang,¹ Chenyang Li², and Francesco A. Evangelista^{1,*}

¹*Department of Chemistry and Cherry Emerson Center for Scientific Computation, Emory University, Atlanta, Georgia 30322, USA*

²*Key Laboratory of Theoretical and Computational Photochemistry, Ministry of Education, College of Chemistry, Beijing Normal University, Beijing 100875, People's Republic of China*

 (Received 19 August 2022; revised 9 November 2022; accepted 14 March 2023; published 24 April 2023)

In this work, we propose a quantum unitary downfolding formalism based on the driven similarity renormalization group (QDSRG) that may be combined with quantum algorithms for both noisy and fault-tolerant hardware. The QDSRG is a classical polynomial-scaling downfolding method that avoids the evaluation of costly three- and higher-body reduced density matrices while retaining the accuracy of classical multireference many-body theories. We calibrate and test the QDSRG on several challenging chemical problems and propose a strategy for reducing the measurement cost. We report QDSRG computations of two chemical systems using the variational quantum eigensolver on IBM quantum devices: (i) the dissociation curve of H₂ using a quintuple- ζ basis and (ii) the bicyclobutane isomerization reaction to *trans*-butadiene, demonstrating the reduction of problems that require several hundred qubits to a single qubit. Our work shows that the QDSRG is a viable approach to leverage near-term quantum devices for estimating molecular properties with chemical accuracy, using only up to the diagonal elements of the two-body reduced density matrix of the reference state.

DOI: [10.1103/PRXQuantum.4.020313](https://doi.org/10.1103/PRXQuantum.4.020313)

I. INTRODUCTION

Molecules and materials that display strong electron correlation are hard to simulate with classical computers due to the exponential growth of the many-body Hilbert space [1]. Quantum computers [2,3] are particularly well suited to simulate many-body systems, as they can efficiently represent and perform operations on many-particle wave functions. These features make them a promising solution to the electron correlation problem [4,5], which, in its most general form, still defies classical algorithms. However, the accurate modeling of realistic many-electron systems requires the use of large computational bases and, therefore, it is unlikely to be accessible to small-scale quantum computers with up to only a few hundred qubits. One of the most promising strategies to maximize the impact of near-term quantum devices is to pair a quantum algorithm with classical approaches that perform a

reduction of the number of qubits required in a quantum computation [6].

Several strategies have been proposed to minimize quantum resources by combining quantum computations with traditional quantum chemistry approaches. Takeshita *et al.* [7] have applied quantum algorithms in combination with the active-space approximation and orbital optimization. This idea has been demonstrated experimentally for model molecules with up to ten orbitals using just two qubits [8]. Boyn *et al.* [9] have obtained active-space 2-RDMs from quantum computations and postprocessed them with two classical correlation methods, the anti-Hermitian contracted Schrödinger equation (ACSE) theory [10–12] and multiconfigurational pair density functional theory [13]. Fujii *et al.* have combined the divide-and-conquer technique with quantum computations to solve the ground state of a 64-qubit two-dimensional Heisenberg model with 20-qubit simulations [14] and have later extended it to obtain excited states of the periodic hydrogen chain [15]. Malone *et al.* have devised an efficient active-space formulation of first-order symmetry-adapted perturbation theory (SAPT) that has produced accurate interaction energies between large molecular systems using low-depth wave functions from quantum computers [16] and, later, Loipersberger *et al.* have extended it to obtain second-order interaction energies [17].

*francesco.evangelista@emory.edu

Published by the American Physical Society under the terms of the [Creative Commons Attribution 4.0 International](https://creativecommons.org/licenses/by/4.0/) license. Further distribution of this work must maintain attribution to the author(s) and the published article's title, journal citation, and DOI.

Tammaro *et al.* [18] have investigated the use of N -electron valence perturbation theory (NEVPT) [19,20] in combination with the variational quantum eigensolver (VQE) [21–23] and quantum subspace expansion [24,25] algorithms. Ryabinkin *et al.* [26] have used low-order perturbative corrections to reduce the quantum resources required in their iterative qubit coupled-cluster VQE approach.

Huggins *et al.* have recently proposed a hybrid algorithm that combines quantum shadow tomography with the auxiliary-field quantum Monte Carlo method, achieving the largest-to-date chemical simulation on hardware of a 16-qubit chemical system [27]. Other works have focused on reducing the number of qubits and gates required by variational quantum algorithms using embedding techniques. For example, density-matrix embedding theory [28,29] has been applied to simulate a H_{10} ring on an ion-trap quantum computer by decomposing this 20-qubit system into ten two-qubit problems [30]. Huang *et al.* have used quantum defect embedding theory to simulate spin defects on quantum computers [31]. Tazhigulov *et al.* have used simplified low-energy spin models and various error-mitigation protocols to simulate iron-sulfur clusters and spin-liquid materials [32]. Combining explicitly correlated methods with quantum algorithms is another strategy explored in several works [33–38] to achieve higher accuracy without increasing quantum resources. Motta *et al.* [33] have used a canonical transcorrelated F12 (CT-F12) Hamiltonian [39] in conjunction with the variational quantum eigensolver method, whereas McArdle *et al.* [34] have used Boys and Handy’s transcorrelated approach, which produces a non-Hermitian Hamiltonian containing up to three-body terms. A recent contribution also considers an *a posteriori* perturbative correction based on the explicitly correlated [2]_{R12} approach [35].

Quantum chemical effective Hamiltonian theories [40–46] offer another way to downfold correlation effects into a small active-space quantum computation. In such approaches, one partitions the orbital space into two sets, active and inactive, and a transformation is applied to the Hamiltonian to eliminate terms that couple these two spaces. The resulting Hamiltonian then accounts for electron correlation effects in the inactive orbitals via effective many-body interactions. In principle, it is straightforward to adapt this strategy to a quantum classical hybrid setting whereby a highly entangled quantum state involving only the active orbitals is solved for on a quantum computer and the remaining weak correlation effects are recovered with a polynomially scaling classical algorithm. However, there are several major potential issues when combining effective Hamiltonian methods and quantum algorithms. A particularly severe limitation of some approaches is the need to measure three- and four-body reduced density matrices (RDMs), introducing a prohibitively large prefactor in quantum computations that scales as the sixth to the eighth

power of the number of active orbitals. A second important issue is the impact of noise in the measured RDMs on the energy (and other properties) and the numerical stability of methods that require the solution of nonlinear equations. Lastly, it is often necessary to go beyond low-order perturbative treatments to achieve accurate energetics. Several quantum downfolding methods have been proposed. The double unitary coupled-cluster (DUCC) approach [47–49] is a downfolding procedure based on a mean-field reference state. Le and Tran [50] have employed their one-body second-order Møller-Plesset perturbation theory (OBMP2) to create an effective Hamiltonian with modified one-body interactions for the VQE method.

This work presents a quantum downfolding approach based on the driven similarity renormalization group (DSRG) [51–54] that addresses the challenges highlighted above, including reducing the cost of measuring RDMs on quantum devices. The DSRG is an integral reformulation of numerical flow-renormalization group methods [55–58]. Our quantum formulation of the DSRG (QDSRG) is compatible with any quantum algorithm capable of producing low-rank RDMs [21,24,59–61] (up to partial or full second order) and augments it with an accurate, intruder-free, and nonperturbative treatment of weak (dynamical) correlation. We benchmark the performance of the QDSRG scheme in computing the dissociation curve of the nitrogen molecule and the adiabatic singlet-triplet splittings of the *para*-benzynes diradical. In addition to exact simulations, we demonstrate the usefulness of this strategy in the presence of realistic noise by combining the QDSRG with VQE experiments on IBM quantum computers. We compute the dissociation curve of the H_2 molecule with a nearly complete quintuple- ζ basis and model the bicyclobutane isomerization pathways to *trans*-butadiene. This isomerization reaction proceeds via two transition states, the relative energies of which are impacted by significant orbital rearrangements and different correlation effects in the electronic states. Resolving the energetics of all reaction intermediates across the full pathway with sufficient accuracy is notoriously challenging for many quantum chemistry methods, including advanced coupled-cluster methods [62]. The methodological advances introduced in this work are complementary to others developed recently to model reactions of ever-increasing complexity on quantum hardware, including the hydrogen-transfer reaction studied at the Hartree-Fock level [63], the recent work of Motta *et al.* [64] on the simulation of ground- and excited-state properties of the sulfonium cation using VQE and quantum subspace expansion [24], and a study by O’Brien *et al.* of the ring-opening reaction in cyclobutadiene using VQE and a Hamiltonian projected on the seniority zero subspace [65]. Our work demonstrates that classical downfolding provides a path to modeling complex chemistry reactivity on near-term quantum devices, accounting for both electron correlation and basis-set effects to approach

relative energies within 1 kcal mol⁻¹ from experimental energies.

II. THEORY

A. Unitary Hamiltonian downfolding via the DSRG

The DSRG method [51–54,66] starts from a reference correlated state Ψ_0 and performs a unitary transformation of the Hamiltonian, H , that brings it to a block-diagonal form

$$H \mapsto \bar{H} = e^{-A} H e^A, \quad (1)$$

where the operator A is anti-Hermitian. The goal of this transformation is to remove the second-quantized components of \bar{H} that couple Ψ_0 to excited configurations, which we refer to as the nondiagonal components of \bar{H} (denoted as \bar{H}^N).

One of the challenges associated with eliminating these couplings (i.e., solving for $\bar{H}^N = 0$) is the emergence of numerical instabilities, which are related to excitations with small energy denominators. To avoid this issue, the DSRG achieves only a partial block diagonalization of H by solving a set of regularized equations

$$\bar{H}^N = R(s). \quad (2)$$

In this equation, $R(s)$ is an operator that depends on the flow parameter $s \in [0, \infty)$, and its purpose is to suppress excited configurations associated with an energy denominator smaller than the energy cutoff $\Lambda = 1/\sqrt{s}$. Hence, solving Eq. (2) imparts a dependence on s onto the A operator and the transformed Hamiltonian.

The DSRG operator $A(s)$ is expressed in terms of a s -dependent coupled-cluster particle-hole excitation operator [67–70] as $A = T - T^\dagger$ with $T = T_1 + T_2 + \dots$, where each k -body component is

$$T_k = \frac{1}{(k!)^2} \sum_{ij\dots}^{\text{hole}} \sum_{ab\dots}^{\text{particle}} t_{ab\dots}^{ij\dots}(s) \{\hat{a}_{ij\dots}^{ab\dots}\}, \quad (3)$$

where we write the normal-ordered creation and annihilation operators in a compact form $\{\hat{a}_{ij\dots}^{ab\dots}\} = \{\hat{a}^a \hat{a}^b \dots \hat{a}_j \hat{a}_i\}$ [71,72] and the cluster amplitudes ($t_{ab\dots}^{ij\dots}$) are tensors that are antisymmetric with respect to the individual permutation of upper and lower indices. The hole space contains the occupied and partially occupied spin orbitals (labeled with the indices i, j, \dots), while the particle space contains the partially occupied and unoccupied spin orbitals (labeled with the indices a, b, \dots) of the reference Ψ_0 . One of the simplest nonperturbative truncation schemes is the linearized DSRG (LDSRG) with one- and two-body operators [LDSRG(2)] [53], where (1) T is truncated as $T \approx$

$T_1 + T_2$ and (2) every commutator in the Baker-Campbell-Hausdorff expansion of \bar{H} contains only one- and two-body operators (indicated with subscript “1,2”) using a linear recursive commutator approximation [41,73]:

$$\bar{H} \approx \bar{H}_{1,2} = H + \sum_{k=1}^{\infty} \frac{1}{k!} \underbrace{[\dots[[H, A]_{1,2}, A]_{1,2}, \dots]_{1,2}}_{k \text{ nested commutators}}. \quad (4)$$

The resulting approximate DSRG-transformed Hamiltonian ($\bar{H}_{1,2}$) contains a scalar term plus one- and two-body interactions, as the original Hamiltonian. We note that it is possible to go beyond this truncation scheme and include higher-order contributions in \bar{H} [74,75]; however, this comes at the cost of increasing the number of unique terms and the computational scaling.

Once Eq. (2) is solved, the energy may be computed as the expectation value of $\bar{H}_{1,2}$:

$$E = \langle \Psi_0 | \bar{H}_{1,2} | \Psi_0 \rangle. \quad (5)$$

Alternatively, one may solve the eigenvalue problem

$$\bar{H}_{1,2} | \tilde{\Psi}_0 \rangle = \tilde{E} | \tilde{\Psi}_0 \rangle \quad (6)$$

and obtain a *relaxed* reference state $\tilde{\Psi}_0$ and its corresponding energy \tilde{E} . It is often the case that multireference quantum chemistry methods, such as CASPT2 [76] or NEVPT2 [19,20], only evaluate the energy as an expectation value via equations analogous to Eq. (5). In this case, one talks of a “diagonalize-then-perturb” approach and the resulting formalism only provides an energy correction rather than a properly downfolded Hamiltonian. We note that when performed exactly, the unitary transformation at the basis of the DSRG [Eq. (1)] would lead to a method similar to the ACSE [10–12]. In the case of a reference composed of a single Slater determinant, the DSRG becomes equivalent to a regularized form of unitary coupled-cluster theory [77].

Solving the DSRG equations [Eq. (2)] requires the reduced density cumulants (RDCs) of the reference state (which we also refer to as “cumulants”) [78,79]. A generic k -body reduced density cumulant (λ_k) is the connected part of the corresponding k -body RDM (γ_k), defined as $\gamma_{uv\dots}^{xy\dots} = \langle \Psi_0 | a_x^\dagger a_y^\dagger \dots a_v a_u | \Psi_0 \rangle$, where the product $a_x^\dagger a_y^\dagger \dots a_v a_u$ contains k creation and k annihilation operators. Throughout the paper, we use the indices u, v, w, x, y , and z to label active spin orbitals partially occupied in Ψ_0 . The RDCs of the reference state encode all the information required to include correlation effects outside of the active orbitals. Therefore, any computational method capable of generating Ψ_0 and its RDMs can be interfaced with the DSRG downfolding procedure. It is convenient to express the DSRG equations in terms of cumulants, as any truncated scheme preserves the size extensivity of the

energy. Reduced density cumulants enter the LDSRG(2) equations in the following way. Evaluation of the operator A requires λ_1 and λ_2 , while evaluation of the energy additionally requires λ_3 , which is challenging to measure on near-term devices. In the next section, we analyze a modified DSRG approach for a hybrid quantum classical scheme.

B. Hybrid quantum classical DSRG downfolding

An outline of how the DSRG downfolding scheme may be adapted to a hybrid quantum classical scheme is illustrated in Fig. 1. We can break the procedure down into four steps:

- (1) *Orbital optimization.* The first step is an optimization of the molecular orbitals for a target electronic state. To ensure that this scheme is applicable to large active spaces, it is important that the cost of the orbital optimization scales as a low-order polynomial of the size of the system. This step could employ a mean-field approximation (e.g., Hartree-Fock) or optimize the orbitals of a correlated state, as in the complete-active-space self-consistent-field (CASSCF) method. In the latter case, a quantum computation may be used to optimize the correlated state.
- (2) *Reference preparation.* In the second step, we propose to employ an approximate reference state that might be obtained from a classical or quantum computation. In this step, the spin orbital basis is partitioned into three subsets: core (doubly occupied), active (partially occupied), and virtual (empty). The quantum computation involves only the active orbitals and uses a modified one-electron operator that accounts for the interaction with the occupied core orbitals. With these restrictions, the quantum computation requires at most $2N_A$ qubits, where N_A is the number of active orbitals. As part of the

quantum computation, the low-rank reduced density cumulants ($\tilde{\lambda}_k$) of the reference state are evaluated. This step requires only a coarsely optimized reference state and, therefore, it does not introduce a significant overhead in our hybrid quantum classical scheme.

- (3) *DSRG downfolding.* The third step consists of a classical DSRG computation using the approximate reduced density cumulants ($\tilde{\lambda}_k$) from step 2. This step produces the anti-Hermitian operator A and the DSRG-transformed Hamiltonian. We also obtain the expectation value of $\bar{H}_{1,2}$ with respect to the approximate RDCs ($(\bar{H}_{1,2})_{\tilde{\lambda}_k}$); however, this quantity is generally a poor approximation to the exact energy. This step has polynomial scaling in the number of active and total orbitals.
- (4) *Eigenvalue estimation.* In the last step of this procedure, the approximate DSRG downfolded Hamiltonian is used in a quantum computation that estimates one of its eigenvalues (\tilde{E}). Depending on the quantum resources available, this step may be performed with a hybrid quantum classical algorithm such as VQE, in which case one may obtain an exact or approximate eigenvalue of $H_{1,2}$, or through the use a pure quantum algorithm such as phase estimation [4,5] to target an exact eigenvalue.

For generality, we separate steps 1 and 2 of the QDSRG scheme; however, if the orbital-optimization step minimizes the energy of a correlated state generated via a quantum computation (e.g., as in CASSCF), then these steps can be combined into a single one.

The most crucial differences between the conventional DSRG formulation and the QDSRG scheme are the density-cumulant approximation in the DSRG downfolding procedure and the eigenvalue estimation (step 4). Here, we consider approximations of the cumulants that are consistent with the measurement of, at most, a quadratic

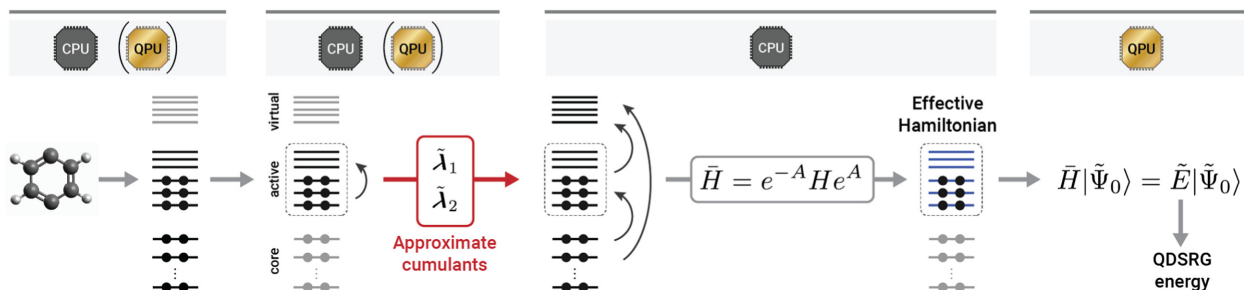


FIG. 1. The QDSRG scheme for performing hybrid quantum classical computations on strongly correlated molecules. The computation begins with a classical or hybrid orbital optimization (1), followed by the preparation of a correlated reference state defined in the subset of active molecular orbitals (2). This step yields the reduced density cumulants ($\tilde{\lambda}_k$), which are passed to a classical DSRG algorithm (3) to produce the effective Hamiltonian ($\bar{H}_{1,2}$) and its expectation value with respect to the approximate cumulants ($(\bar{H}_{1,2})_{\tilde{\lambda}_k}$). In the last step (4), an eigenvalue of the DSRG effective Hamiltonian is found via a quantum algorithm.

scaling number of elements. The simplest approximation (1-QDSRG) retains only the diagonal elements of the one-body density cumulant, that is,

$$\tilde{\lambda}_v^u = \begin{cases} \lambda_u^u, & \text{if } u = v, \\ 0, & \text{otherwise.} \end{cases} \quad (7)$$

Since $\lambda_1 = \boldsymbol{\gamma}_1$, this scheme requires only the diagonal parts of the one-body density matrix $\gamma_u^u = \langle \Psi_0 | a_u^\dagger a_u | \Psi_0 \rangle$. As the number operators $n_u = a_u^\dagger a_u$ commute with each other, the diagonal elements of arbitrary-rank RDMs can be measured simultaneously. Therefore, if Ψ_0 is generated via a quantum computation, this would require performing only two experiments to measure the energy ($\langle H \rangle$) and the diagonal elements of $\boldsymbol{\gamma}_1$.

The next approximation (2-QDSRG) requires access to a quadratic number of elements of the RDCs and consists in taking the full one-body density matrix ($\tilde{\lambda}_1 = \lambda_1$) plus the diagonal components of the two-body reduced density cumulant

$$\tilde{\lambda}_{xy}^{uv} = \begin{cases} \lambda_{uv}^{uv}, & \text{if } u = x \text{ and } v = y, \\ \lambda_{vu}^{uv} = -\lambda_{uv}^{uv}, & \text{if } u = y \text{ and } v = x, \\ 0, & \text{otherwise.} \end{cases} \quad (8)$$

These cumulant approximations may be justified using a perturbative argument. At first order in perturbation theory (assuming a one-body diagonal zeroth-order operator, $H_0 = \sum_p \epsilon_p \{a_p^\dagger a_p\}$), one may show that the amplitudes corresponding to single and double excitations are given by [52]

$$t_a^{i,(1)} = [f_a^i + \sum_{ux} \Delta_{ux}^{x,ij,(1)} \gamma_u^x] \frac{1 - e^{-s(\Delta_a^i)^2}}{\Delta_a^i}, \quad (9)$$

$$t_{ab}^{ij,(1)} = \langle ab || ij \rangle \frac{1 - e^{-s(\Delta_{ab}^{ij})^2}}{\Delta_{ab}^{ij}}, \quad (10)$$

where the quantities f_a^i and $\langle ab || ij \rangle$ are elements of an effective one-body operator and antisymmetrized two-electron integrals, respectively, while the denominators are defined as $\Delta_a^i = \epsilon_i - \epsilon_a$ and $\Delta_{ab}^{ij} = \epsilon_i + \epsilon_j - \epsilon_a - \epsilon_b$, with $\epsilon_i = f_i^i$ [52]. These equations show that at first order, the double-excitation component of A is independent of the reference cumulants, and the single-excitation component of A depends only on the off-diagonal elements of the active-active block of $\boldsymbol{\gamma}_1$ [since when $x = u$ in Eq. (9), we have that $\gamma_u^u \Delta_u^u = \gamma_u^u (\epsilon_u - \epsilon_u) = 0$]. Therefore, the 2-QDSRG method is already consistent with a first-order approximation to the DSRG operator A , while 1-QDSRG neglects the off-diagonal terms of γ_u^x that enter into Eq. (9). The three-body cumulant λ_3 is neglected in both the 1-QDSRG and 2-QDSRG approximations and it may be

shown to enter the energy at second-order in perturbation theory. The impact of neglecting λ_3 in the DSRG has been analyzed in previous studies [52,80,81].

It is noteworthy that the QDSRG scheme significantly reduces the cost of state preparation and measurement. As shown by Zhao *et al.* [82], the number of repeated state preparations required to estimate the k -body RDM of a n -fermion system with precision ϵ can be reduced to $\binom{n}{k} k^{3/2} \log(n) / \epsilon^2$ via partial tomography. As other active-space methods, the QDSRG scheme reduces n from the full basis to a limited number of active spin orbitals. More importantly, a significant cost reduction is achieved compared to other active-space methods that require up to the 4-RDM ($k = 4$) [18] and the LDSRG(2) method, which requires up to the 3-RDM ($k = 3$). In the linearized 1-QDSRG with one- and two-body operators [1-QLDSRG(2)], the diagonal elements of 1-RDM can be measured with a cost independent of n , while the 2-QLDSRG(2) corresponds to the case $k = 1$ with the small additional cost of measuring the diagonal elements of the 2-RDM (independent of n), which needs $(n \log(n) + 1) / \epsilon^2$ state preparations and measurements for a desired precision ϵ .

Note that the computational cost of the DSRG classical downfolding procedure (step 3) is also reduced by the cumulant approximation introduced in the QDSRG scheme. Specifically, the N_A^6 -scaling terms are eliminated completely in QLDSRG(2), compared to the original LDSRG(2) formalism. However, we should point out that this cost reduction is limited, since the overall scaling of the QLDSRG(2) transformation is still dominated by a term that scales as $\mathcal{O}(N_V^4 N_C^2)$, where N_V is the number of unoccupied orbitals and N_C the number of doubly occupied orbitals.

To enable the pipeline of QDSRG computations, we implement functionalities that export integrals and read or write the reference density matrices from external files in FORTE [83], an open-source plugin for the *ab initio* quantum chemistry package PSI4 [84]. We obtain the QDSRG effective Hamiltonian from FORTE using a spin-free implementation [66].

III. CALIBRATION

A. Noiseless simulations

To investigate the accuracy of the QDSRG procedure for quantum computing, we examine a numerical example. We consider the H_2 molecule at four geometries using a triple- ζ basis. As the H_2 molecule is stretched, the $1\sigma_g$ and $1\sigma_u$ orbitals become near degenerate and the reference state must be taken of the form $|\Psi_0\rangle = c_g |(1\sigma_g)^2\rangle + c_u |(1\sigma_u)^2\rangle$ to guarantee a continuous and qualitatively correct solution for all bond lengths. Table I reports the energy error with respect to a full configuration interaction (FCI) computation for the LDSRG(2) and the QLDSRG(2) methods. We

TABLE I. The energy error for the H_2 molecule (in mE_h) computed with the LDSRG(2) and QLDSRG(2) methods. All computations use a cc-pVTZ basis [85] and the flow parameter value $s = 0.5 E_h^{-2}$. The energy errors are computed with respect to the full configuration interaction (FCI) energies (in E_h) reported in the last row of the table. For the LDSRG(2), the expectation value of the energy is designated with “ $\langle \bar{H}_{1,2} \rangle$,” while the lowest eigenvalue is indicated with “eig. $\bar{H}_{1,2}$.” For the QDSRG methods, we report two sets of data. Those labeled “ $\gamma_3 = 0$ ” use an approximate three-body cumulant reconstructed from $\tilde{\lambda}_1$ and $\tilde{\lambda}_2$. The results for line M employ CCSD natural orbitals and the one-body relaxed CCSD reduced density matrix as input to the QDSRG procedure.

Case	Method	Orbital type	Active orbitals	r_{H-H} (Å)			
				0.75	1.50	2.25	3.00
A	LDSRG(2) ($\langle \bar{H}_{1,2} \rangle$)	RHF	$\{1\sigma_g, 1\sigma_u\}$	0.306	7.337	15.454	17.428
B	LDSRG(2) ($\langle \bar{H}_{1,2} \rangle$)	CASSCF(2,2)	$\{1\sigma_g, 1\sigma_u\}$	0.791	1.007	0.307	0.041
C	LDSRG(2) ($\langle \bar{H}_{1,2} \rangle$)	CASSCF(2,2)	$\{1\sigma_g, 1\sigma_u, 2\sigma_g, 2\sigma_u\}$	0.064	0.280	0.080	0.012
D	LDSRG(2) (eig. $\bar{H}_{1,2}$)	CASSCF(2,2)	$\{1\sigma_g, 1\sigma_u\}$	0.331	0.070	0.242	0.041
E	2-QLDSRG(2) ($\gamma_3 = 0$)	CASSCF(2,2)	$\{1\sigma_g, 1\sigma_u\}$	0.327	0.055	0.235	0.039
F	2-QLDSRG(2)	CASSCF(2,2)	$\{1\sigma_g, 1\sigma_u\}$	1.065	2.981	2.152	0.354
G	1-QLDSRG(2) ($\gamma_3 = 0$)	CASSCF(2,2)	$\{1\sigma_g, 1\sigma_u\}$	2.455	6.422	4.591	1.203
H	1-QLDSRG(2) ($\gamma_3 = 0$)	CASSCF(2,2)	$\{1\sigma_g, 1\sigma_u, 2\sigma_g, 2\sigma_u\}$	0.601	2.193	1.383	0.564
I	1-QLDSRG(2) ($\gamma_3 = 0$)	CASSCF(2,2)	$\{1\sigma_g, 1\sigma_u, 2\sigma_g, 2\sigma_u, 3\sigma_g, 3\sigma_u\}$	0.324	0.511	0.071	-0.051
J	1-QLDSRG(2)	CASSCF(2,2)	$\{1\sigma_g, 1\sigma_u\}$	1.061	2.732	1.890	0.327
K	1-QLDSRG(2)	CASSCF(2,2)	$\{1\sigma_g, 1\sigma_u, 2\sigma_g, 2\sigma_u\}$	0.016	1.392	0.935	0.070
L	1-QLDSRG(2)	CASSCF(2,2)	$\{1\sigma_g, 1\sigma_u, 2\sigma_g, 2\sigma_u, 3\sigma_g, 3\sigma_u\}$	-0.104	0.293	0.130	0.008
M	1-QLDSRG(2)	CCSD NOs	$\{1\sigma_g, 1\sigma_u\}$	1.059	2.927	2.095	0.351
	FCI	RHF	All MOs	-1.172 301	-1.066 168	-1.010 114	-1.000 726

report both the average energy $\langle \bar{H}_{1,2} \rangle$ and the eigenvalue of $\bar{H}_{1,2}$ using active spaces of various sizes and different choices of orbitals. In addition to the $1\sigma_g$ and $1\sigma_u$ orbitals, which originate from the $1s$ shell, we consider active spaces augmented with the $2\sigma_g/2\sigma_u$ and $3\sigma_g/3\sigma_u$ orbitals (of mixed $2s/2p_z$ character). These are found to be the orbitals that give the most important energetic contributions at the equilibrium and stretched geometries. Active spaces that span the full $2s$ and $2p$ shells (including the $1\pi_u$ and $1\pi_g$ MOs) do not improve the energetics in a consistent way. In analyzing these results, we focus on the largest error and use the labels A–M to refer to a specific row of Table I.

The importance of optimizing the orbitals is reflected in the significant difference in the accuracy of the LDSRG(2) ($\langle \bar{H}_{1,2} \rangle$) when the orbitals $1\sigma_g$ and $1\sigma_u$ come from a restricted Hartree-Fock (RHF) or CASSCF calculation (using only the $1\sigma_g$ and $1\sigma_u$ as active MOs), whereby the latter optimizes both the orbitals and coefficients of the determinants that define Ψ_0 . The LDSRG(2) error with RHF orbitals (A) is as large as $17.4 mE_h \approx 0.47$ eV (at $r_{H-H} = 3$ Å), whereas CASSCF orbitals (B) give an error of approximately $1 mE_h \approx 0.03$ eV, and this error can be further reduced to less than $0.3 mE_h$ (C) if the reference state is augmented with determinants formed out of a larger active space that includes the $2\sigma_g$ and $2\sigma_u$ orbitals. Diagonalization of $\bar{H}_{1,2}$ in an active space containing the $1\sigma_g$ and $1\sigma_u$ MOs (D) yields a maximum error similar to the one of case (C). Note that even with a full iterated solution of the equations, the LDSRG(2) method is not exact for two electrons and the potential-energy curve of H_2 will deviate from FCI.

This deviation is due to both truncation of the commutator expansion of \bar{H} and the use of a finite value of s .

For the QDSRG methods, we report two sets of results. We first examine the ones denoted with “ $\gamma_3 = 0$,” which use a three-body cumulant ($\tilde{\lambda}_3$) reconstructed from $\tilde{\lambda}_1$ and $\tilde{\lambda}_2$ [78,79,86,87] and, therefore, differ slightly from the approximations defined in the previous section, where we set $\tilde{\lambda}_3 = 0$. The case $\gamma_3 = 0$ is consistent with the fact that a reference containing two electrons always yields a zero three-body RDM. Since the three-body cumulant contains disconnected contributions from products of the one- and two-body RDMs, its elements may be nonzero even for two-electron systems [79]. We note that the 2-QDSRG approach (E) leads to small errors (maximum $0.4 mE_h$) that are similar to those of case D, where the energy comes from diagonalization of the LDSRG(2) $\bar{H}_{1,2}$. When we neglect the three-body cumulant (F) entirely, the 2-QDSRG error increases for all points. This observation may be understood by considering how $\tilde{\lambda}_3$ enters into the DSRG equations. At the lowest order, $\tilde{\lambda}_3$ gives a scalar contribution to $\bar{H}_{1,2}$ via the term $1/4\lambda_{uvw}^{xyz}(\langle mz||uv \rangle t_{xy}^{mw} + \langle we||xy \rangle t_{ez}^{uv})$, where implicit summation of repeated indices is assumed and m and e run over all the doubly occupied and empty orbitals, respectively. We estimate this quantity using second-order perturbation theory and find that it explains the difference between the $\gamma_3 = 0$ and $\tilde{\lambda}_3 = 0$ energies of H_2 (and, therefore, also provides a means of correcting for this difference). For example, at $r = 1.50$ Å, the contribution due to $\tilde{\lambda}_3$ amounts to about $-2.77 mE_h$, a value close to minus the energy-error increase (about $2.93 mE_h$) seen between E and F.

The more drastic approximation (1-QDSRG) with $\gamma_3 = 0$ gives a large maximum error (6.4 mE_h , G). In this case, it is possible to improve the accuracy by expanding the active space with a single or double set of σ_g/σ_u orbitals, reducing the maximum energy errors to 2.2 and 0.5 mE_h (H, I), respectively.

Interestingly, imposing $\tilde{\lambda}_3 = 0$ has a different impact on the 1-QDSRG, improving the agreement with FCI, an effect attributed to error cancellation. The different behavior of the “1-” and “2-” approximations going from $\gamma_3 = 0$ to $\tilde{\lambda}_3 = 0$ (e.g., E versus F and G versus J) is a consequence, in the latter case, of $\tilde{\lambda}_2$ not being included in the reconstruction of $\tilde{\lambda}_3$.

As mentioned earlier, a practical realization of the QDSRG scheme requires either two quantum computations (one to generate the orbitals and approximate cumulants plus a final diagonalization step) or it may use orbitals and cumulants from a polynomial-scaling classical method as a starting point. Here, we demonstrate how this second option may be realized in practice using natural orbitals from coupled-cluster theory [88]. In the results labeled “M,” we use coupled-cluster theory with singles and doubles (CCSD) to compute an approximate unrelaxed density matrix γ_1^{CCSD} that spans the entire orbital space. The orbitals are then rotated to the natural basis (defined as the basis in which γ_1^{CCSD} is diagonal). The active-space occupation numbers are then scaled so that their sum equals to the number of electrons in the active orbitals (2) and these are used to reconstruct an approximate diagonal $\tilde{\lambda}_1$. The 1-QLDSRG(2) computations using CCSD natural orbitals (NOs) (M) give energies that are comparable to those using CASSCF(2,2) orbitals (J), with the energy difference between these two approximate methods being at most 0.2 mE_h at $r_{\text{HH}} = 1.50$ Å. We reexamine the use of CCSD NOs as a way to reduce the cost of QDSRG computations in Sec. IV.

In Appendix B, we provide a comparison of the QDSRG scheme with the DUCC downfolding approach for the H_2 molecule and the beryllium (Be) atom using data from Ref. [47]. Both methods employ an exponential unitary transformation of the Hamiltonian but they differ in several ways. For example, whereas the DUCC is formulated in a single-reference setting, the QDSRG method derives the A operator from a correlated state. This and other differences have important consequences on the accuracy of these two methods, with our comparison showing that the QDSRG leads to smaller errors (up to an order of magnitude smaller), especially in computations with fewer active orbitals.

B. Sensitivity to noise

We conclude our initial assessment of the QDSRG approach by analyzing the sensitivity to stochastic errors introduced by quantum devices. As shown in Fig. 1, step

2 of the QDSRG procedure allows for the approximate cumulants to be obtained from a quantum computation. In this case, there will be a compounding of errors due to the fact that the measured densities (later converted into cumulants) will be subject to finite measurement errors and gate and measurement noise.

To study the effect of noise on the measured RDMs, we perform QDSRG computations on the H_2 molecule at bond distances of 0.75 and 1.5 Å. Following Ref. [89], we model noise by augmenting the cumulants with stochastic error sampled from a Gaussian distribution with standard deviation σ and zero mean [$\mathcal{N}(0, \sigma^2)$],

$$\gamma_{xy\dots}^{uv\dots, \text{measured}} = \gamma_{xy\dots}^{uv\dots} + \mathcal{N}(0, \sigma^2). \quad (11)$$

This simple noise model can mimic finite measurement errors but cannot account for correlated noise among qubits and decoherence. Noise is added to the unique elements of the RDMs to avoid breaking antisymmetry with respect to permutation of the upper and lower indices (e.g., $\gamma_{xy}^{uv} = -\gamma_{xy}^{vu} = -\gamma_{yx}^{uv} = \gamma_{yx}^{vu}$); however, we do not enforce fermionic N -representability conditions [90–93] onto the resulting RDMs, which likely leads to overestimation of the resulting energy errors. Several works discuss how to utilize the N -representability constraints to accelerate and improve hybrid quantum algorithms, mainly via reducing the measurement scaling [63,94], which might be combined with the QDSRG approach to improve its accuracy.

Figure 2 shows the energy error computed with respect to noiseless results for the 1- and 2-QLDSRG(2) schemes (enforcing $\gamma_3 = 0$). At both geometries, we observe that the 1-QLDSRG(2) is less sensitive to noise than the 2-QLDSRG(2) and that the average energy error increases linearly with σ . Interestingly, the average error is slightly higher at the shorter bond distance (0.75 Å) than at the elongated one (1.5 Å). In both cases, a value of $\sigma = 0.01$ seems sufficient to recover the energy with an error less than 1 kcal/mol (approximately 1.6 mE_h), a threshold often referred to as *chemical accuracy*. These results can then inform an analysis of the quantum resources necessary to measure the RDMs with an accuracy sufficient for a hybrid quantum classical procedure based on the QDSRG.

In summary, the preliminary results reported in Secs. III A and III B show that even a very drastic approximation of the cumulants that enter the DSRG *combined with* diagonalization of the resulting transformed Hamiltonian can yield energies with small absolute energy errors, even in the presence of noise. We expand this analysis to molecules with more complex electronic structures and larger basis sets in Sec. IV, with the goal of determining if it is possible to predict relative energies that approach chemical accuracy. There, we also report the results of experiments on NISQ devices that show the potential usefulness of QDSRG in leveraging near-term quantum computers.

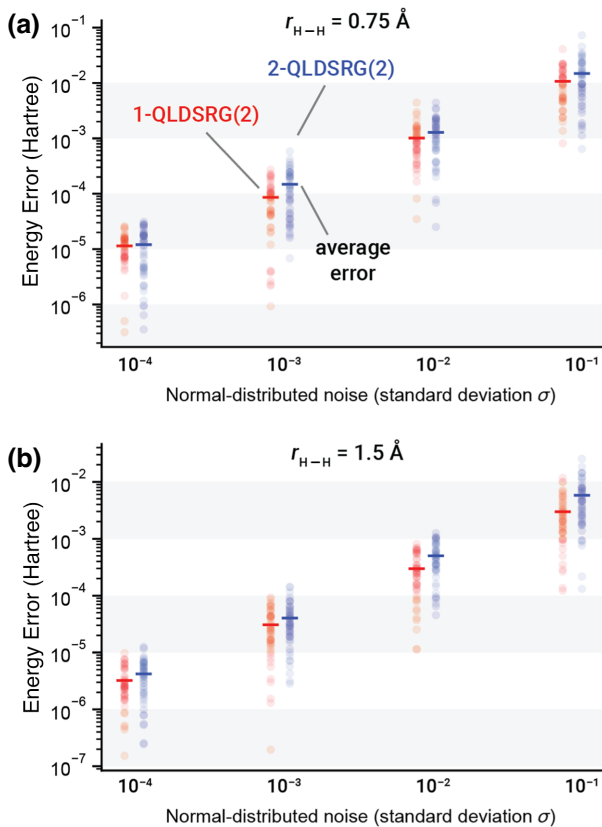


FIG. 2. The energy error for the H_2 molecule (in mE_h) computed with the QLDSRG(2) with various amounts of stochastic noise (σ) added to the RDMs. For a given value of σ , the semiopaque circles aligned vertically show the distribution of errors from 50 computations, while the horizontal bars represent the average error. All computations use a cc-pVTZ basis [85] and the flow parameter value $s = 0.5 E_h^{-2}$. The energy errors are computed with respect to noiseless values. The data are obtained imposing $\gamma_3 = 0$ in the reconstruction of the approximate three-body cumulant.

IV. RESULTS AND DISCUSSION

In this section, we report two types of QDSRG results: the noiseless exact computations in Secs. IV A and IV B and device computations (Sec. IV C) where we combine the QDSRG with variational quantum computations performed on IBM hardware.

A. Dissociation curve of the nitrogen molecule

As the first benchmark of the QDSRG scheme, we compute the potential-energy curve for the ground singlet state of N_2 using an active space containing six orbitals (built from combinations of the six $2p$ N orbitals). Figure 3(a) shows the potential-energy curve for the LDSRG(2), the two approximate variants of the QDSRG, CCSD [97], and CCSD(T) [98]. In the DSRG computations, we employ CASSCF(6,6) orbitals and use the corresponding state as a reference, while the CCSD and CCSD(T) results employ

restricted (RHF) and unrestricted broken-symmetry (UHF) Hartree-Fock references. The DSRG methods produce curves that are nearly indistinguishable, except in the recoupling region (1.6–2.0 Å), where the QDSRG energy is slightly higher than the LDSRG(2) one. The RHF-CCSD and RHF-CCSD(T) curves, although accurate in the equilibrium region, deviate significantly from the DSRG one for large $N-N$ distances, while the UHF-based counterparts give results that are close to the DSRG methods. In the bottom panel of Fig. 3, we report the energy error with respect to FCI and the nonparallelism error (NPE), defined as the difference between the largest and smallest energy deviation from FCI along the dissociation curve. Here, we note that the 1- and 2-QLDSRG(2) lead to errors as large as 17.5 mE_h (and NPE as high as 14.4 mE_h), while the LDSRG(2) is more accurate, with the maximum deviation

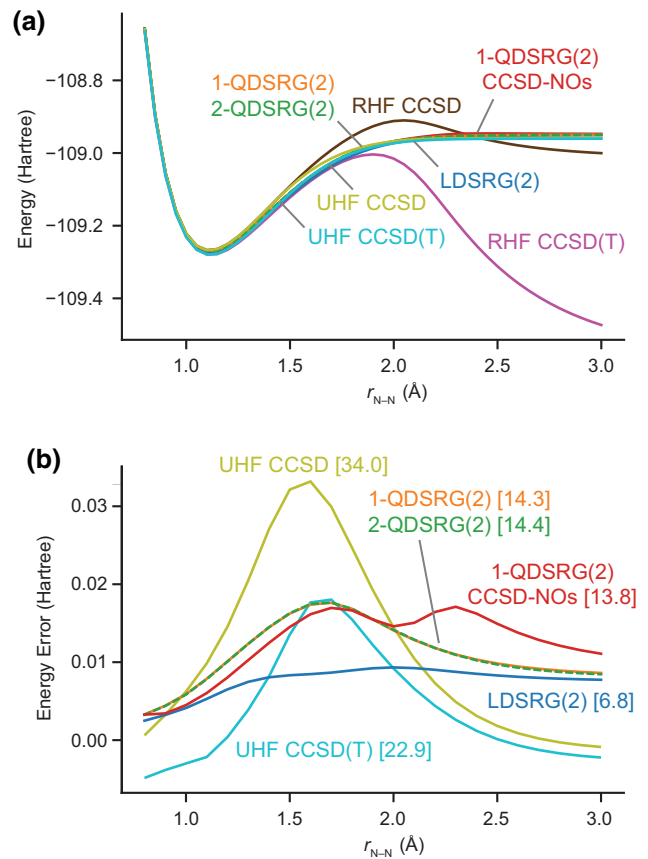


FIG. 3. The dissociation curve for the ground-state N_2 computed with the LDSRG(2) and QLDSRG(2). (a) The total energy and (b) the energy error with respect to FCI in units of E_h . Nonparallelism errors (in mE_h) for each method are reported in square brackets. All computations use an active space containing six $2p$ N atomic orbitals, a cc-pVDZ basis [85], and the flow parameter value $s = 0.5 E_h^{-2}$. The 1-QLDSRG(2)-CCSD data employ natural orbitals and γ_1 from CCSD as the input to the QDSRG computation. All other results employ CASSCF(6,6) orbitals.

TABLE II. Spectroscopic constants for the ground state ($X^1\Sigma_g^+$) of N_2 from the dissociation curves in Fig. 3. The data in parentheses show deviations from FCI results. All LDSRG(2) and QLDSRG(2) computations as well as the literature results listed here use the cc-pVDZ basis.

Method	r_e (Å)	ω_e (cm $^{-1}$)	$\omega_e x_e$ (cm $^{-1}$)	D_e (eV)
LDSRG(2)	1.1177 (−0.0024)	2344.6 (21.0)	15.0 (0.1)	8.766 (0.054)
2-QLDSRG(2)	1.1159 (−0.0042)	2365.2 (41.6)	14.8 (−0.1)	8.712 (0.000)
1-QLDSRG(2)	1.1159 (−0.0042)	2364.9 (41.3)	14.8 (−0.1)	8.716 (0.004)
1-QLDSRG(2) CCSD NOs	1.1165 (−0.0036)	2365.6 (42.0)	15.3 (0.4)	8.834 (0.122)
UHF-CCSD	1.1123 (−0.0078)	2411.7 (88.2)	14.0 (−0.9)	8.396 (−0.316)
UHF-CCSD(T)	1.1184 (−0.0017)	2341.9 (18.3)	14.6 (−0.3)	8.700 (−0.012)
DMRG(6,6)-tCCSD ^a	1.1180 (−0.0022)	2327.0 (3.4)
MRCISD ^b	1.1192 (−0.0010)	2330.1 (6.5)	14.9 (−0.0)	...
MRCISD+Q ^b	1.1204 (0.0002)	2321.4 (−2.2)	14.9 (−0.0)	...
FCI	1.1202	2323.6	14.9	8.712

^aFrom Ref. [95].

^bFrom Ref. [96].

from FCI always being less than $10 mE_h$. As observed for H_2 , the 1-QLDSRG(2) potential-energy curve based on the CCSD-NOs reference is still accurate and displays maximum errors with respect to FCI smaller than those obtained using CASSCF orbitals and cumulants from exact diagonalization. In comparison, the UHF-based CCSD and CCSD(T) curves show larger deviations from FCI, with NPE values (22.9 and 34.0 mE_h) larger than those of the 1- and 2-QLDSRG(2) (14.3 and 14.4 mE_h).

Table II reports various spectroscopic constants, including the bond distance (r_e), the harmonic vibrational frequency (ω_e), the anharmonicity constant ($\omega_e x_e$), and the bond dissociation energy (D_e , electronic energy only) for the ground state ($X^1\Sigma_g^+$) of N_2 computed from the potential-energy curves in Fig. 3, as well as values from other methods, including the density-matrix renormalization group [99] tailored coupled-cluster theory with a CAS(6e,6o) active space [DMRG(6,6)-tCCSD] [95], MRCI with singles and doubles (MRCISD) [100,101], and MRCISD with Davidson’s correction (MRCISD+Q) [102]. Notably, all LDSRG(2) and QLDSRG(2) computations yield results that considerably exceed the quality of the UHF-CCSD ones for all constants and dissociation energies, while the LDSRG(2) achieves an accuracy comparable to UHF-CCSD(T). While LDSRG(2) predicts an equilibrium bond length r_e similar to the DMRG(6,6)-tCCSD one, both LDSRG(2) and 2-QLDSRG(2) overestimate the vibrational constant ω_e .

B. Singlet-triplet gaps of *para*-benzynes

In our next example, we apply the QDSRG scheme to a medium-sized molecule. We compute the adiabatic singlet-triplet splitting ($\Delta E_{ST} = E_T - E_S$) of *para*-benzynes. The singlet ground state of this molecule exhibits a pronounced diradical character and is dominated by two closed-shell determinants. *para*-benzynes and its isomers have

been studied extensively both experimentally [105] and theoretically [103,104,106,110–115].

Here, we compute the singlet-triplet splitting using CASSCF(2,2) orbitals for the singlet state and ROHF orbitals for the triplet state. The experimental splitting value is taken from the ultraviolet photoelectron spectroscopy results of Ref. [105]. We utilize the singlet and triplet geometries from Ref. [104], which are optimized at the Mk-MRCCSD/cc-pVTZ level of theory. All computations use the cc-pVTZ basis set [85] and the value of the DSRG flow parameter is set to $1.0 E_h^{-2}$, based on previous studies [80,96,116]. We freeze the six $1s$ -like orbitals on carbon atoms in the DSRG correlation treatment.

Table III reports the singlet-triplet splitting obtained by the LDSRG(2) and the QLDSRG(2) methods. All splittings are shifted by $+0.30$ kcal mol $^{-1}$ to account for zero-point vibrational energy (ZPVE) corrections [103]. The labels for the methods are consistent with those in Table I.

It is encouraging that most LDSRG(2) and QLDSRG(2) results are chemically accurate (deviation from experimental value less than 1 kcal mol $^{-1}$), with the largest deviation reaching 1.04 kcal mol $^{-1}$. For all QLDSRG(2) variants, the estimated ΔE_{ST} deviates from the LDSRG(2) (eig. $\bar{H}_{1,2}$) value by only 0.03–0.50 kcal mol $^{-1}$, which shows the robustness of the DSRG downfolding with respect to density-cumulant approximations even for medium-sized systems. Interestingly, the simpler 1-QLDSRG(2) method more accurately estimates ΔE_{ST} (3.38 kcal mol $^{-1}$) than the 2-QLDSRG(2) (2.98 kcal mol $^{-1}$), likely due to error cancellation. For comparison, we also include in Table III theoretical ΔE_{ST} values from other methods, including Mukherjee’s multireference coupled-cluster theory with singles, doubles, and perturbative triples [Mk-MRCCSD(T)] [104], internally contracted multireference coupled-cluster theory [ic-MRCCSD(T)] [106], double ionization potential and double electron attachment equation-of-motion

TABLE III. Adiabatic singlet-triplet splittings ($\Delta E_{ST} = E_T - E_S$) (in kcal mol⁻¹) of *para*-benzynes computed with the LDSRG(2) and QLDSRG(2) in the cc-pVTZ basis [85] with the flow parameter value $s = 1.0 E_h^{-2}$. The data in parentheses show the difference with respect to the experimental value of ΔE_{ST} (in kcal mol⁻¹). All LDSRG(2) and QLDSRG(2) results include a zero-point vibrational energy (ZPVE) correction equal to +0.30 kcal mol⁻¹ (see Ref. [103]). The geometries are taken from Ref. [104]. We use CASSCF(2,2) optimized orbitals for all computations of the singlet state and ROHF orbitals for the triplet state. For the LDSRG(2), the expectation value of the energy is designated with “ $\langle \bar{H}_{1,2} \rangle$,” while the lowest eigenvalue is indicated with “eig. $\bar{H}_{1,2}$.” For the QDSRG methods, we report two sets of data. Those labeled “ $\gamma_3 = 0$ ” use an approximate three-body cumulant reconstructed from approximate $\tilde{\lambda}_1$ and $\tilde{\lambda}_2$. All literature results listed here for comparison use the same cc-pVTZ basis.

Method	ΔE_{ST} (kcal mol ⁻¹)
Active orbitals: $\{\sigma_g, \sigma_u\}$	
CASSCF(2,2)	0.31 (−3.49)
LDSRG(2) ($\langle \bar{H}_{1,2} \rangle$)	2.76 (−1.04)
LDSRG(2) (eig. $\bar{H}_{1,2}$)	3.48 (−0.32)
2-QLDSRG(2) ($\gamma_3 = 0$)	3.45 (−0.35)
1-QLDSRG(2) ($\gamma_3 = 0$)	3.22 (−0.58)
2-QLDSRG(2)	2.98 (−0.82)
1-QLDSRG(2)	3.38 (−0.42)
Mk-MRCCSD(T) ^{b,g}	4.45 (+0.65)
ic-MRCCSD(T) ^{c,g}	5.18 (+1.38)
DIP-EOM-CCSD ^f	4.40 (+0.60)
DEA-EOM-CCSD ^{e,h}	3.83 (+0.03)
SF-CCSD ^{d,h}	3.87 (+0.07)
Experiment ^a	3.8 ± 0.4

^aFrom Ref. [105]; experimental value taken from ultraviolet photoelectron spectra of *para*-benzynes radical anion.

^bFrom Ref. [104].

^cFrom Ref. [106].

^dFrom Ref. [107].

^eFrom Ref. [108].

^fFrom Ref. [109].

^gA ZPVE correction of +0.30 kcal mol⁻¹ obtained using CCSD(T)/cc-pVDZ (see Ref. [103]) is included, the same as that used for LDSRG(2) and QLDSRG(2).

^hA ZPVE correction of 0.021 eV (+0.48 kcal mol⁻¹) at the SF-DFT/6-311G* level (see Ref. [110]) is included according to the paper.

coupled-cluster theory with singles and doubles (DIP-EOM-CCSD [107] and DEA-EOM-CCSD [108]), and spin-flip coupled-cluster theory with singles and doubles (SF-CCSD) [109,110]. In general, both LDSRG(2) and QLDSRG(2) slightly underestimate ΔE_{ST} , while the other methods tend to overestimate it by 0.03–1.38 kcal mol⁻¹. Most QLDSRG(2) splittings are more accurate than those from Mk-MRCCSD(T), ic-MRCCSD(T), and DIP-EOM-CCSD, while DEA-EOM-CCSD and SF-CCSD slightly outperform the other methods.

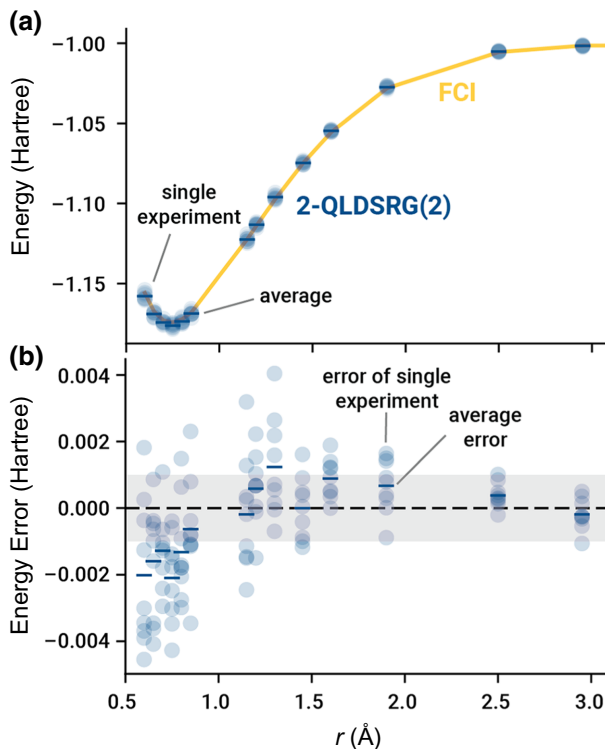


FIG. 4. (a) The dissociation curve and (b) the energy error for the H₂ molecule computed with the 2-QLDSRG(2) using one qubit on the IBM_LAGOS device. The energy errors are with respect to FCI energies. For each geometry, the semiopaque blue circles aligned vertically show the distribution of energies (energy errors) from nine experiments, with each experiment consisting of 32 000 measurements, while the horizontal bars in blue denote average energies or average energy errors. All computations use the cc-pV5Z basis [85] (110 basis functions), CASSCF(2,2) orbitals, and the flow parameter value $s = 0.5 E_h^{-2}$. The gray-shaded area indicates unsigned energy errors below 1 mE_h. The unsigned energy errors and the standard deviations are reported in Table IV.

C. Hardware implementation

In this section, we combine the 2-QLDSRG(2) method with the VQE [21–23] on the IBM quantum computers to demonstrate the ability of this hybrid scheme to compute the total energies under realistic noise from near-term quantum devices. We use the QISKIT [117] package to construct circuits and execute them on hardware.

Ideally, we would measure both density matrices and the QDSRG energy (steps 2 and 4 in Fig. 1) from a quantum computation. Due to the high level of noise from near-term devices and the fact that density matrices are more sensitive to noise than the energy, we employ a quantum computer only to estimate the eigenvalue of the 2-QLDSRG(2) effective Hamiltonian $\bar{H}_{1,2}$. We use the VQE algorithm to optimize a trial wave function and measure its energy. To reduce the quantum resources (the number of qubits, the circuit depth, etc.) and minimize errors,

TABLE IV. The errors of 2-QLDSRG(2) energies in mE_h (with respect to FCI energies) along the H_2 dissociation curve (Fig. 4). For results from the IBM_LAGOS device, we show the unsigned average energy errors and standard deviations (in mE_h). Unsigned energy errors below $1 mE_h$ are highlighted in bold type.

$r/\text{\AA}$	$\Delta E_{\text{noiseless}}$	ΔE_{device}	Standard deviation
0.6	0.53	2.02	2.08
0.65	0.54	1.59	1.63
0.7	0.54	1.28	1.14
0.75	0.55	2.10	1.24
0.8	0.54	1.32	1.41
0.85	0.54	0.63	1.47
1.15	0.40	0.19	1.61
1.2	0.37	0.59	1.00
1.3	0.32	1.24	1.42
1.45	0.28	0.00	0.89
1.6	0.29	0.89	0.56
1.9	0.36	0.68	0.77
2.5	0.20	0.38	0.35
2.95	0.07	0.19	0.45
6.0	0.00	0.31	0.15

we explore a symmetry-preserving one-qubit ansatz (for details, see Appendix A).

For each experiment on the device, we carry out the maximum number of measurements allowed, which differs by device. To ameliorate measurement errors, we utilize readout-error-mitigation tools in the QISKIT-IGNIS module to construct a calibration matrix and apply its inverse to the raw measurement counts of each experiment.

Our first example is a computation of the dissociation curve of H_2 , which is a representative benchmark system for quantum computing. Figure 4 shows the dissociation curve and the energy error for the H_2 molecule in the cc-pVTZ basis [85] (110 orbitals) obtained by the one-qubit 2-QLDSRG(2) computations on the IBMQ_LAGOS quantum computer. A direct second-quantized quantum computation would require 220 qubits (ignoring qubit tapering or other symmetry-adaptation techniques). We also report the 2-QLDSRG(2) energy errors and the standard deviations of the device results in Table IV. The effectiveness of the QDSRG downfolding method can be seen from the small errors of the 2-QLDSRG(2) energies, which differ from noiseless simulations at most by $0.5 mE_h$ for all geometries. The 2-QLDSRG(2) energies from the device have unsigned average errors lower than $1 mE_h$ for over half of the geometries, with a maximum error of $2.0 mE_h$. Empirically, it is important to collect the measurement statistics of 10^5 shots to obtain a reliable estimate of the average energy from the device. We observe that device results have relatively large errors for short bond distances. This is due to the behavior of the matrix element c_z in the qubit Hamiltonian, which enters via the term $c_z Z$ [see Eq.

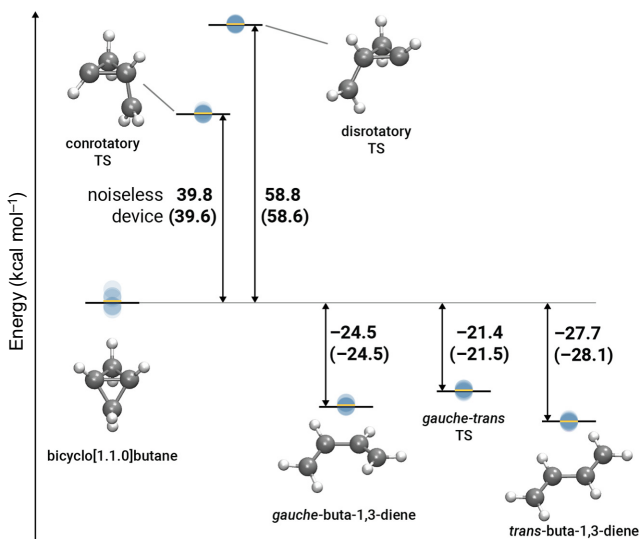


FIG. 5. Conrotatory and disrotatory pathways describing the isomerization of bicyclo[1.1.0]butane (bicyclobutane) to *trans*-buta-1,3-diene (*trans*-butadiene). The enthalpies (in kcal mol^{-1}) are relative to the reactant for relevant stationary points computed with the 2-QLDSRG(2) method using one qubit on the device IBMQ_MANILA. The black horizontal bars represent the 2-QLDSRG(2) results obtained with noiseless simulations. The device results are shown in parentheses. The semiopaque blue circles aligned vertically show the distribution of the relative enthalpies from eight experiments (20 000 measurements per experiment), while the yellow horizontal bars denote the average relative enthalpies. We use a cc-pVTZ basis [85] (204 basis functions) and CASSCF(2,2) natural orbitals and the flow parameter value $s = 1.0 E_h^{-2}$ for all six stationary points.

(A5) in Appendix A]. By definition, c_z is half the energy difference between the $(1\sigma_g)^2$ and $(1\sigma_u)^2$ electron configurations generated by the VQE trial state. As the H_2 bond is stretched and the two configurations become near degenerate, c_z decreases by several orders of magnitude (-0.819 at 0.70\AA , while -0.036 for 2.95\AA), reducing the impact of the error in the estimation of the expectation value of Z at large r values.

From this example, we see that errors from hardware (finite measurements, decoherence, etc.) are more significant than errors from the QDSRG downfolding.

For our second set of hardware experiments, we consider a larger and more chemically relevant problem, the pericyclic rearrangement reaction of bicyclo[1.1.0]butane (bicyclobutane) to *trans*-buta-1,3-diene (*trans*-butadiene). This isomerization process goes through a concerted conrotatory movement of the methylene groups with an activation barrier (enthalpy) of $40.6 \pm 2.5 \text{ kcal mol}^{-1}$ [120], suggested by early experimental studies [120,122–125]. This mechanism has been investigated in many computational studies using high-level electronic structure methods, including MRMBPT [118,126,127], multireference

TABLE V. LDSRG(2) and QLDSRG(2) (exact and device) computations of the relative enthalpies (in kcal mol⁻¹) with respect to the bicyclobutane reactant of the conrotatory transition state and the disrotatory transition state, the *gauche*-butadiene intermediate, the transition state connecting *gauche*-butadiene and *trans*-butadiene, and the *trans*-butadiene product. We use the cc-pVTZ basis [85] (204 basis functions) and CASSCF(2,2) natural orbitals and the flow parameter value $s = 1.0 E_h^{-2}$. All results include zero-point vibrational energy (ZPVE) corrections taken from Ref. [118]. The OMR3-DMC and CC(t;3) results also use the cc-pVTZ basis. The differences of values (in kcal mol⁻¹) with respect to the experimental data for the conrotatory transition state and *trans*-butadiene are shown in parentheses; values within 1 kcal mol⁻¹ deviation are indicated in bold type.

	Conrotatory TS	Disrotatory TS	<i>Gauche</i> -butadiene	<i>Gauche-trans</i> TS	<i>Trans</i> -butadiene
LDSRG(2) ($\langle \bar{H}_{1,2} \rangle$)	41.3 (0.7)	58.5	-24.5	-21.5	-27.7 (-1.8)
LDSRG(2) (eig. $\bar{H}_{1,2}$)	39.6 (-1.0)	58.6	-24.5	-21.4	-27.8 (-1.9)
		2-QLDSRG(2)			
Exact	41.5 (0.9)	58.9	-24.3	-21.3	-27.5 (-1.6)
IBMQ_MANILA ^a	42.6 (2.0)	57.8	-23.8	-22.2	-27.4 (-1.5)
IBMQ_LAGOS ^b	42.7 (2.1)	59.6	-23.3	-20.7	-26.4 (-0.5)
IBMQ_JAKARTA ^c	40.5 (-0.1)	57.5	-25.6	-22.4	-28.4 (-2.5)
		2-QLDSRG(2) ($\gamma_3 = 0$)			
Exact	39.8 (-0.8)	58.8	-24.5	-21.4	-27.7 (-1.8)
IBMQ_MANILA ^a	39.6 (-1.0)	58.6	-24.5	-21.5	-28.1 (-2.2)
IBMQ_LAGOS ^b	39.0 (-1.6)	57.7	-25.2	-22.2	-28.6 (-2.7)
IBMQ_JAKARTA ^c	39.1 (-1.5)	58.4	-25.2	-21.7	-28.0 (-2.1)
OMR3-DMC ^d	40.4(5)	58.6(5)	-25.2(5)	-22.2(5)	-27.9(5)
CC(t;3) ^e	40.2	60.1	-25.3	-22.6	-28.3
Experiment	40.6 ± 2.5 ^f				-25.9 ± 0.4 ^g

^aThe average is over 8 experiments (20 000 shots per experiment).

^bThe average is over 10 experiments (32 000 shots per experiment).

^cThe average is over 10 experiments (20 000 shots per experiment).

^dFrom Ref. [119].

^eFrom Ref. [62].

^fFrom Ref. [120].

^gThe reaction enthalpy at 298 K is based on enthalpies of the formation of bicyclo[1.1.0]butane and buta-1,3-diene reported in Ref. [121].

configuration interaction (MRCI) [127], variants of single-reference coupled-cluster methods including CR-CC(2,3) [118,128] and CC(t;3) [62], the diffusion quantum Monte Carlo method [119], and the anti-Hermitian contracted Schrödinger equation (ACSE) method [126,129].

These theoretical studies also investigate the unfavored concerted disrotatory pathway [118,119,126–128], characterized by a transition state (TS) that is estimated to be 15–25 kcal mol⁻¹ higher in energy than the conrotatory one. Both transition states display significant biradical character [118] and their ground-state wave functions have large contributions from multiple determinants, requiring a multireference treatment. This makes the system suitable for treatment with the QDSRG method. Previous studies have also confirmed that for both concerted pathways, the reaction reaches a *gauche*-buta-1,3-diene intermediate (*gauche*-butadiene) and then proceeds through a low-energy rotational barrier to the *trans*-butadiene product.

We compute the reaction enthalpies along the full concerted conrotatory and disrotatory pathways from bicyclobutane to *trans*-butadiene. The Cartesian coordinates of the structures of all six stationary points optimized at

the CASSCF(10,10)/cc-pVDZ level of theory are taken from Ref. [118]. Zero-point vibrational energies (ZPVE) obtained at the same level of theory are used to convert total electronic energies to enthalpies. For all six stationary points, we use CASSCF(2,2) natural orbitals, which yield a two-configuration reference that can be mapped to a one-qubit ansatz (for details, see Appendix A). All computations use the cc-pVTZ basis [85] (204 orbitals) and we freeze four 1s-like orbitals on carbon atoms in the DSRG correlation treatment.

Figure 5 shows the concerted conrotatory and disrotatory pathways of the bicyclobutane → *trans*-butadiene reaction and Table V reports the relative enthalpies (with respect to the bicyclobutane reactant) from the LDSRG(2) and the 2-QLDSRG(2) methods obtained via noiseless simulations and via VQE on three quantum devices. We show the best device results, obtained with the IBMQ_MANILA device, in Fig. 5.

Compared to the experimental value [120], both LDSRG(2) and the 2-QLDSRG(2) methods give relative enthalpies of the conrotatory transition state that achieve chemical accuracy, while the relative enthalpies of *trans*-butadiene predicted by the two methods are slightly

underestimated [121]. For the other three stationary points, experimental data are not available; therefore, we compare our results with data from two high-level approaches, the optimized multireference diffusion quantum Monte Carlo (OMR3-DMC) [119] and an active-space coupled-cluster method with corrected triple excitations, termed CC(t;3) [62], using the same cc-pVTZ basis. The relative enthalpy of the disrotatory transition state predicted by the LDSRG(2) and 2-QLDSRG(2) methods agrees with the OMR3-DMC result (58.6 kcal mol⁻¹) [119] and is slightly lower than the CC(t;3) value (60.1 kcal mol⁻¹) [62]. For both *gauche*-butadiene and the transition state connecting *gauche*-butadiene and *trans*-butadiene, the LDSRG(2) and the 2-QLDSRG(2) results are about 1 kcal mol⁻¹ lower than the OMR3-DMC and CC(t;3) values. The 2-QLDSRG(2) results from three devices are in good agreement with the result from noiseless simulations, with most devices yielding values within 1 kcal mol⁻¹ from the exact result. Notably, two devices yield chemically accurate relative enthalpies for the conrotatory transition state (40.5 kcal mol⁻¹, 39.6 kcal mol⁻¹). The best device results (data obtained with the IBMQ_MANILA device) in Table V give unsigned errors less than 0.5 kcal mol⁻¹ for all six stationary points.

The results for the bicyclobutane \rightarrow *trans*-butadiene reaction demonstrate that the QDSRG method can effectively downfold the dynamical correlation for a large basis with 204 orbitals, reducing the number of qubits from several hundred to just one.

V. CONCLUSIONS

In this work, we introduce a practical unitary downfolding method that enables accurate molecular computations on near-term quantum computers. The QDSRG is agnostic to the type of quantum algorithm (e.g., variational, phase estimation) and can be used with both noisy near-term computers and future fault-tolerant hardware. Therefore, we expect that the QDSRG will be a useful method to leverage small quantum computers in applications to large molecules and large basis sets.

The QDSRG is based on the DSRG [51], a classical numerically robust and polynomial-scaling approach to block diagonalizing many-body Hamiltonians. In this work, we propose a “diagonalize-then-dress-then-diagonalize” strategy that combines truncation of the reduced density cumulants provided to the DSRG with diagonalization of the resulting similarity-transformed Hamiltonian. This downfolding procedure may be justified by a perturbative analysis of the DSRG equations and leads to two practical computational schemes: in the 1-QDSRG, we retain only the diagonal part of the one-body RDM, whereas in the 2-QDSRG, we retain the full one-body RDM and the diagonal part of the two-body cumulants. These two schemes require the estimation of a number of

reduced density-matrix elements that are at most linear or quadratic in the number of active orbitals (N_A), substantially reducing the demands of conventional multireference theories, which require N_A^6 to N_A^8 RDM elements.

Our calibration of the QDSRG shows that the use of orbitals optimized for a reference correlated state is crucial to compute accurate energies. The QDSRG results show that the “2-” approximation is able to accurately predict energies along the bond-breaking coordinate in a minimal active space. The “1-” approximation leads to larger errors but these can be suppressed by increasing the active-space size. To simulate the effect of noise, we examine QDSRG computations starting with inaccurate RDMs and find that milliHartree accuracy can be retained when the standard deviation of the RDMs errors is as large as 10^{-3} – 10^{-2} .

In our computations on the more challenging N₂ and *p*-benzynes molecules, we are also able to accurately predict potential-energy curves and singlet-triplet gaps using the QDSRG. In the case of N₂, we demonstrate how the first two steps of the QDSRG procedure (orbital optimization and reference preparation) can be approximated with the classical polynomial-scaling CCSD method, using the corresponding one-body reduced density matrix. Finally, we demonstrate the QDSRG procedure in combination with the VQE algorithm on the IBM quantum devices. We extend computations of the H₂ dissociation curve with a nearly complete quintuple- ζ basis, corresponding to a full computation with 220 qubits. In this example, we find that hardware errors still remain the most significant source of error in comparison to the QDSRG downfolding error. We also apply the QDSRG method to model the reaction pathways of the bicyclobutane \rightarrow *trans*-butadiene isomerization process using a basis of 204 orbitals. We are able to obtain high-quality device results that reach sub-kcal mol⁻¹ accuracy with respect to the exact QDSRG and two high-level classical electronic structure approaches with a modest number of measurements, while a full VQE computation may need 10⁹ measurements for one single energy evaluation based on the empirical resource estimation of Ref. [130].

The extensions of the QDSRG with explicit correlation methods and to electronically excited states are two interesting directions that are worth exploring. We expect that with the availability of more accurate hardware and a larger number of qubits, the QDSRG will provide a systematic path to perform accurate quantum chemistry computations on chemically relevant systems.

ACKNOWLEDGMENTS

This work was supported by the U.S. Department of Energy under Award No. DE-SC0019374. This research was supported in part by the National Science Foundation under Grant No. NSF PHY-1748958. We thank Nicholas Stair and Nan He for their contributions to the definition

and implementation of the integral exchange format in FORTE and Jonathon Misiewicz, Eugene DePrince, and Tom O'Brien for helpful conversations.

APPENDIX A: SYMMETRY-PRESERVING ANSATZ FOR TWO-CONFIGURATION WAVE FUNCTIONS

We exploit spin, particle number, and spatial symmetries to construct a hardware-efficient ansatz for two-configuration wave functions. Consider a two-electron wave function in a basis of two molecular orbitals ψ_1, ψ_2 . The singlet ground state in the most general case includes three configurations (bars over the number denote β spin orbitals),

$$\begin{aligned} |\Phi_1\rangle &= |\psi_1\psi_{\bar{1}}\rangle, \\ |\Phi_2\rangle &= |\psi_2\psi_{\bar{2}}\rangle, \\ |\Phi_3\rangle &= \frac{1}{\sqrt{2}}(|\psi_1\psi_{\bar{2}}\rangle - |\psi_{\bar{1}}\psi_2\rangle). \end{aligned} \quad (\text{A1})$$

We can remove the contribution of the open-shell configuration $|\Phi_3\rangle$ from the normalized ground-state wave function $|\Psi_0\rangle = C'_1|\Phi_1\rangle + C'_2|\Phi_2\rangle + C'_3|\Phi_3\rangle$ without changing the energy via an orbital rotation

$$\begin{aligned} |\psi'_1\rangle &= \cos\theta|\psi_1\rangle + \sin\theta|\psi_2\rangle, \\ |\psi'_2\rangle &= \sin\theta|\psi_1\rangle - \cos\theta|\psi_2\rangle, \end{aligned} \quad (\text{A2})$$

where $\tan 2\theta = \sqrt{2}C'_3/(C'_1 - C'_2)$ [103,131,132]. For detailed discussions on this basis transformation, we refer interested readers to Sec. IV of Ref. [103].

For H_2 , the ground-state wave function expanded in the CASSCF(2,2) orbitals can be accurately described by two closed-shell configurations, while for two transition states in the bicyclobutane \rightarrow *trans*-butadiene reaction, the open-shell contribution to the wave function cannot be neglected due to the strong biradical character (especially for the disrotatory TS). Therefore, we transform to the CASSCF(2,2) natural orbital basis, which is mathematically equivalent to enforcing Eq. (A2). The ground states of the other four stationary points in the pathways are generally well described by a single determinant in the CASSCF(2,2) basis; however, for consistency, we employ CASSCF(2,2) natural orbitals for all computations.

The resulting two-configuration wave function $|\Psi_0\rangle = C_1|\psi'_1\psi'_{\bar{1}}\rangle + C_2|\psi'_2\psi'_{\bar{2}}\rangle$ can be mapped to a one-qubit space

$$\begin{aligned} |\psi'_1\psi'_{\bar{1}}\rangle &\rightarrow |0\rangle, \\ |\psi'_2\psi'_{\bar{2}}\rangle &\rightarrow |1\rangle, \end{aligned} \quad (\text{A3})$$

which leads to the one-qubit wave function ansatz

$$|\Psi\rangle = C_1|0\rangle + C_2|1\rangle. \quad (\text{A4})$$

TABLE VI. The relations between the elements of the fermionic 1-RDM ($\gamma_q^p = \langle a_p^\dagger a_q \rangle$) and 2-RDM ($\gamma_{rs}^{pq} = \langle a_p^\dagger a_q^\dagger a_s a_r \rangle$) and the measured quantities for the one-qubit ansatz. Only nonzero elements are shown; others are zero due to symmetries. $|C_1|^2 = \langle \Psi|0\rangle\langle 0|\Psi\rangle$ and $|C_2|^2 = \langle \Psi|1\rangle\langle 1|\Psi\rangle$ are obtained from projective measurements of the optimized state in the computational basis; $\langle X \rangle$ is the expectation value of the Pauli X operator.

RDM element	Analytical	Measurement
$\gamma_1^1, \gamma_{\bar{1}}^{\bar{1}}, \gamma_{1\bar{1}}^{\bar{1}\bar{1}}, \gamma_{\bar{1}\bar{1}}^{\bar{1}\bar{1}}$	$\cos^2 t/2$	$ C_1 ^2$
$\gamma_2^2, \gamma_{\bar{2}}^{\bar{2}}, \gamma_{2\bar{2}}^{\bar{2}\bar{2}}, \gamma_{\bar{2}\bar{2}}^{\bar{2}\bar{2}}$	$\sin^2 t/2$	$ C_2 ^2$
$\gamma_{1\bar{1}}^{\bar{1}\bar{1}}, \gamma_{\bar{1}\bar{1}}^{\bar{1}\bar{1}}$	$-\cos^2 t/2$	$- C_1 ^2$
$\gamma_{2\bar{2}}^{\bar{2}\bar{2}}, \gamma_{\bar{2}\bar{2}}^{\bar{2}\bar{2}}$	$-\sin^2 t/2$	$- C_2 ^2$
$\gamma_{2\bar{2}}^{\bar{1}\bar{1}}, \gamma_{\bar{2}\bar{2}}^{\bar{1}\bar{1}}, \gamma_{1\bar{1}}^{\bar{2}\bar{2}}, \gamma_{\bar{1}\bar{1}}^{\bar{2}\bar{2}}$	$\cos t/2 \sin t/2$	$\langle X \rangle / 2$
$\gamma_{2\bar{2}}^{\bar{1}\bar{1}}, \gamma_{\bar{2}\bar{2}}^{\bar{1}\bar{1}}, \gamma_{1\bar{1}}^{\bar{2}\bar{2}}, \gamma_{\bar{1}\bar{1}}^{\bar{2}\bar{2}}$	$-\cos t/2 \sin t/2$	$-\langle X \rangle / 2$

This state can be prepared by applying to the $|0\rangle$ state a single Y -rotation gate $\hat{R}_Y(t) = e^{-itY/2}$ with one variational parameter t , giving $C_1 = \cos(t/2)$, $C_2 = \sin(t/2)$. The Hamiltonian in the one-qubit basis is represented as $H = h_{00}|0\rangle\langle 0| + h_{11}|1\rangle\langle 1| + h_{10}(|0\rangle\langle 1| + |1\rangle\langle 0|)$, where h_{00} , h_{11} , and h_{10} are calculated from the one- and two-electron integrals. The Hamiltonian can be decomposed into a weighted sum of single-qubit Pauli operators

$$H = c_0 + c_z Z + c_x X, \quad (\text{A5})$$

with coefficients given by $c_0 = (h_{00} + h_{11})/2$, $c_z = (h_{00} - h_{11})/2$, and $c_x = h_{10}$.

The expectation value of this one-qubit Hamiltonian with respect to $|\Psi\rangle$ has the definite tomography [133,134] given by

$$\langle H \rangle_t = a + b \cos t + c \sin t. \quad (\text{A6})$$

The coefficients a , b , and c can be found using a three-point Fourier quadrature [133] that requires measuring expectation values for three parameters, t_0 , t_1 , and t_2 . The corresponding linear equation to solve is

$$\begin{pmatrix} 1 & \langle Z \rangle_{t_0} & \langle X \rangle_{t_0} \\ 1 & \langle Z \rangle_{t_1} & \langle X \rangle_{t_1} \\ 1 & \langle Z \rangle_{t_2} & \langle X \rangle_{t_2} \end{pmatrix} \begin{pmatrix} a \\ b \\ c \end{pmatrix} = \begin{pmatrix} \langle H \rangle_{t_0} \\ \langle H \rangle_{t_1} \\ \langle H \rangle_{t_2} \end{pmatrix}.$$

In this work, we use the following three-point Fourier quadrature:

$$t_0, t_0 - \pi/3, t_0 + \pi/3, \quad (\text{A7})$$

where t_0 is arbitrary. For convenience, we use the analytical solution for the optimal angle

$$t_0 = \arctan 2(c_x, c_z). \quad (\text{A8})$$

TABLE VII. A comparison of the energy errors (in mE_h) of the QDSRG and the DUCC for the H_2 molecule at four bond lengths in the cc-pVTZ basis, using DSRG flow parameter $s = 0.5 E_h^{-2}$. The size of the active space is denoted in parentheses. The energy errors are with respect to the full-space (30-orbital) FCI computations [absolute energies (in E_h) are shown in the first row]. The DUCC data are taken from Ref. [47].

Method	Orbital type (N_{act})	0.8 a.u.	1.4008 a.u.	4.00 a.u.	10.00 a.u.
FCI (full space)	RHF (30)	-1.015 729	-1.172 455	-1.014 872	-0.999 623
FCI (active space)	RHF (4)	32.729	25.755	7.872	2.523
DUCC	RHF (4)	7.129	4.555	-0.328	-1.977
LDSRG(2) (diag. $\tilde{H}_{1,2}$)	RHF (4)	-0.130	-0.234	1.920	0.122
1-QLDSRG(2)	RHF (4)	-0.094	-0.098	4.047	0.524
2-QLDSRG(2)	RHF (4)	-0.087	-0.084	3.794	0.126
1-QLDSRG(2)	CASSCF(2,2) (4)	0.455	0.169	1.498	0.006
2-QLDSRG(2)	CASSCF(2,2) (4)	0.460	0.179	1.662	0.006

For the reference preparation (step 2 in Fig. 1), we run the VQE algorithm to obtain the 1- and 2-RDMs. These quantities can be measured from the state tomography of the optimal wave function. Table VI summarizes the expressions for the 1- and 2-RDMs in terms of analytical expressions of the variational parameter t and quantities from direct measurements.

Note that for both the 1- and 2-QDSRG methods, we only need to measure the Pauli Z operator to compute the full 1-RDM and the approximate 2-RDM, while the Pauli X operator only contributes to the nondiagonal components of the two-body reduced density cumulant. Finally, we use the VQE algorithm to estimate the eigenvalue of the DSRG effective Hamiltonian (step 4 in Fig. 1).

APPENDIX B: COMPARISONS WITH THE DOUBLE-UNITARY COUPLED-CLUSTER APPROACH

Here, we compare our QDSRG method with the DUCC downfolding technique for the H_2 molecule and the Be atom. In Table VII, we report energies of H_2 at four geometries obtained by diagonalizing the bare, the QDSRG-downfolded, and the DUCC downfolded Hamiltonians in a four-orbital active space, together with the energy errors with respect to the full-space FCI results, which use 30 orbitals. We also compute QDSRG energies using different types of orbitals. The DUCC data are taken from Ref. [47]. We observe that for three geometries, all QDSRG computations consistently give less significant energy errors than the DUCC results. For instance, the largest error for the DUCC using RHF orbitals is $7.13 mE_h$, while the QDSRG shows smaller errors (at most $4.1 mE_h$). The use of CASSCF orbitals further reduces the maximum QDSRG errors to at most $1.7 mE_h$.

Table VIII shows the comparison of the Be atom results using active spaces of different sizes and three basis sets. Here, we see that the DUCC method introduces errors in the range of $18\text{--}30.5 mE_h$ when five or six active orbitals

are used and that this error is reduced to smaller values ($1.8\text{--}7.3 mE_h$) when using nine active orbitals, while QDSRG results consistently show much smaller energy errors ($0.9\text{--}4.9 mE_h$) for all active spaces and basis sets. Notably, the QDSRG downfolding is most effective for the large cc-pVQZ basis, which significantly reduces the energy errors of the active-space FCI results by 50, 50.2, and $26 mE_h$ for five-, six-, and nine-orbital active spaces, while the DUCC method merely gives a reduction of 24, 27, and $19 mE_h$.

TABLE VIII. A comparison of the energy errors (in mE_h) of the QDSRG and the DUCC for the Be atom with different basis sets and active spaces. The DSRG flow parameter $s = 2.0 E_h^{-2}$. All computations use RHF orbitals. The energy errors are with respect to the full-space FCI computations [absolute energies (in E_h) are shown in the last column], which use 14, 30, and 55 orbitals for the cc-pVDZ, cc-pVTZ, and cc-pVQZ basis sets, respectively. The DUCC data are taken from Ref. [47].

Method	Five orbitals	Six orbitals	Nine orbitals	All orbitals
cc-pVDZ				
FCI	22.242	20.575	0.493	-14.617 409
DUCC	19.009	18.109	1.809	
1-QLDSRG(2)	3.408	1.998	3.067	
2-QLDSRG(2)	3.430	2.074	3.065	
cc-pVTZ				
FCI	34.881	33.621	7.024	-14.623 810
DUCC	26.710	24.410	5.010	
1-QLDSRG(2)	4.199	3.202	1.216	
2-QLDSRG(2)	4.200	3.192	2.751	
cc-pVQZ				
FCI	54.950	54.366	26.798	-14.640 147
DUCC	30.547	27.547	7.347	
1-QLDSRG(2)	4.927	4.166	0.879	
2-QLDSRG(2)	4.923	4.158	2.909	

- [1] R. B. Laughlin and D. Pines, The theory of everything, *Proc. Natl. Acad. Sci. USA* **97**, 28 (2000).
- [2] R. P. Feynman, Simulating physics with computers, *Int. J. Theor. Phys.* **21**, 467 (1982).
- [3] Y. I. Manin, *Computable and Uncomputable* [in Russian] (Sovetskoye Radio, Moscow, 1980); see *Mathematics as Metaphor: Selected Essays of Yuri I. Manin* (American Mathematical Society, Providence, 2007), pp. 77–78 for an English translation.
- [4] D. S. Abrams and S. Lloyd, Simulation of Many-Body Fermi Systems on a Universal Quantum Computer, *Phys. Rev. Lett.* **79**, 2586 (1997).
- [5] D. S. Abrams and S. Lloyd, Quantum Algorithm Providing Exponential Speed Increase for Finding Eigenvalues and Eigenvectors, *Phys. Rev. Lett.* **83**, 5162 (1999).
- [6] B. Bauer, D. Wecker, A. J. Millis, M. B. Hastings, and M. Troyer, Hybrid Quantum-Classical Approach to Correlated Materials, *Phys. Rev. X* **6**, 031045 (2016).
- [7] T. Takeshita, N. C. Rubin, Z. Jiang, E. Lee, R. Babbush, and J. R. McClean, Increasing the Representation Accuracy of Quantum Simulations of Chemistry without Extra Quantum Resources, *Phys. Rev. X* **10**, 011004 (2020).
- [8] M. Urbanek, D. Camps, R. Van Beeumen, and W. A. de Jong, Chemistry on quantum computers with virtual quantum subspace expansion, *J. Chem. Theory Comput.* **16**, 5425 (2020).
- [9] J.-N. Boyn, A. O. Lykhin, S. E. Smart, L. Gagliardi, and D. A. Mazziotti, Quantum-classical hybrid algorithm for the simulation of all-electron correlation, *J. Chem. Phys.* **155**, 244106 (2021).
- [10] D. A. Mazziotti, Anti-Hermitian Contracted Schrödinger Equation: Direct Determination of the Two-Electron Reduced Density Matrices of Many-Electron Molecules, *Phys. Rev. Lett.* **97**, 143002 (2006).
- [11] S. E. Smart and D. A. Mazziotti, Quantum Solver of Contracted Eigenvalue Equations for Scalable Molecular Simulations on Quantum Computing Devices, *Phys. Rev. Lett.* **126**, 070504 (2021).
- [12] S. E. Smart, J.-N. Boyn, and D. A. Mazziotti, Resolving correlated states of benzyne with an error-mitigated contracted quantum eigensolver, *Phys. Rev. A* **105**, 022405 (2022).
- [13] G. Li Manni, R. K. Carlson, S. Luo, D. Ma, J. Olsen, D. G. Truhlar, and L. Gagliardi, Multiconfiguration pair-density functional theory, *J. Chem. Theory Comput.* **10**, 3669 (2014).
- [14] K. Fujii, K. Mizuta, H. Ueda, K. Mitarai, W. Mizukami, and Y. O. Nakagawa, Deep Variational Quantum Eigensolver: A Divide-and-Conquer Method for Solving a Larger Problem with Smaller Size Quantum Computers, *PRX Quantum* **3**, 010346 (2022).
- [15] K. Mizuta, M. Fujii, S. Fujii, K. Ichikawa, Y. Imamura, Y. Okuno, and Y. O. Nakagawa, Deep variational quantum eigensolver for excited states and its application to quantum chemistry calculation of periodic materials, *Phys. Rev. Res.* **3**, 043121 (2021).
- [16] F. D. Malone, R. M. Parrish, A. R. Welden, T. Fox, M. Degroote, E. Kyoseva, N. Moll, R. Santagati, and M. Streif, Towards the simulation of large scale protein-ligand interactions on NISQ-era quantum computers, *Chem. Sci.* **13**, 3094 (2022).
- [17] M. Loipersberger, F. Malone, R. M. Parrish, A. R. Welden, T. Fox, M. Degroote, E. Kyoseva, N. Moll, R. Santagati, and M. Streif, Accurate non-covalent interaction energies on noisy intermediate-scale quantum computers via second-order symmetry-adapted perturbation theory, *Chem. Sci.* (2023).
- [18] A. Tammara, D. E. Galli, J. E. Rice, and M. Motta, N -electron valence perturbation theory with reference wave functions from quantum computing: Application to the relative stability of hydroxide anion and hydroxyl radical, *J. Phys. Chem. A* **127**, 817 (2023).
- [19] C. Angeli, R. Cimiraglia, S. Evangelisti, T. Leininger, and J. P. Malrieu, Introduction of n -electron valence states for multireference perturbation theory, *J. Chem. Phys.* **114**, 10252 (2001).
- [20] C. Angeli, M. Pastore, and R. Cimiraglia, New perspectives in multireference perturbation theory: The n -electron valence state approach, *Theor. Chem. Acc.* **117**, 743 (2007).
- [21] A. Peruzzo, J. McClean, P. Shadbolt, M.-H. Yung, X.-Q. Zhou, P. J. Love, J. L. O. r. Brien, and A. Aspuru-Guzik, A variational eigenvalue solver on a photonic quantum processor, *Nat. Commun.* **5**, 4213 (2014).
- [22] M.-H. Yung, J. Casanova, L. Lamata, E. Solano, A. Aspuru-Guzik, J. R. McClean, and A. Mezzacapo, From transistor to trapped-ion computers for quantum chemistry, *Sci. Rep.* **4**, 3589 (2014).
- [23] J. R. McClean, J. Romero, R. Babbush, and A. Aspuru-Guzik, The theory of variational hybrid quantum-classical algorithms, *New J. Phys.* **18**, 023023 (2016).
- [24] J. R. McClean, M. E. Kimchi-Schwartz, J. Carter, and W. A. de Jong, Hybrid quantum-classical hierarchy for mitigation of decoherence and determination of excited states, *Phys. Rev. A* **95**, 042308 (2017).
- [25] J. I. Colless, V. V. Ramasesh, D. Dahlen, M. S. Blok, M. E. Kimchi-Schwartz, J. R. McClean, J. Carter, W. A. de Jong, and I. Siddiqi, Computation of Molecular Spectra on a Quantum Processor with an Error-Resilient Algorithm, *Phys. Rev. X* **8**, 011021 (2018).
- [26] I. G. Ryabinkin, A. F. Izmaylov, and S. N. Genin, *A posteriori* corrections to the iterative qubit coupled cluster method to minimize the use of quantum resources in large-scale calculations, *Quantum Sci. Technol.* **6**, 024012 (2021).
- [27] W. J. Huggins, B. A. O’Gorman, N. C. Rubin, D. R. Reichman, R. Babbush, and J. Lee, Unbiasing fermionic quantum Monte Carlo with a quantum computer, *Nature* **603**, 416 (2022).
- [28] G. Knizia and G. K.-L. Chan, Density Matrix Embedding: A Simple Alternative to Dynamical Mean-Field Theory, *Phys. Rev. Lett.* **109**, 186404 (2012).
- [29] S. Wouters, C. A. Jiménez-Hoyos, Q. Sun, and G. K.-L. Chan, A practical guide to density matrix embedding theory in quantum chemistry, *J. Chem. Theory Comput.* **12**, 2706 (2016).
- [30] Y. Kawashima, E. Lloyd, M. P. Coons, Y. Nam, S. Matsuura, A. J. Garza, S. Johri, L. Huntington, V. Senicourt,

- A. O. Maksymov, J. H. V. Nguyen, J. Kim, N. Alidoust, A. Zaribafiyani, and T. Yamazaki, Optimizing electronic structure simulations on a trapped-ion quantum computer using problem decomposition, *Commun. Phys.* **4**, 245 (2021).
- [31] B. Huang, M. Govoni, and G. Galli, Simulating the Electronic Structure of Spin Defects on Quantum Computers, *PRX Quantum* **3**, 010339 (2022).
- [32] R. N. Tazhigulov, S.-N. Sun, R. Haghshenas, H. Zhai, A. T. Tan, N. C. Rubin, R. Babbush, A. J. Minnich, and G. K. Chan, Simulating challenging correlated molecules and materials on the Sycamore quantum processor (2022), arXiv preprint [ArXiv:2203.15291](https://arxiv.org/abs/2203.15291).
- [33] M. Motta, T. P. Gujarati, J. E. Rice, A. Kumar, C. Masteran, J. A. Latone, E. Lee, E. F. Valeev, and T. Y. Takeshita, Quantum simulation of electronic structure with a transcorrelated Hamiltonian: Improved accuracy with a smaller footprint on the quantum computer, *Phys. Chem. Chem. Phys.* **22**, 24270 (2020).
- [34] S. McArdle and D. P. Tew, Improving the accuracy of quantum computational chemistry using the transcorrelated method (2020), arXiv preprint [ArXiv:2006.11181](https://arxiv.org/abs/2006.11181).
- [35] P. Schleich, J. S. Kottmann, and A. Aspuru-Guzik, Improving the accuracy of the variational quantum eigensolver for molecular systems by the explicitly-correlated perturbative $[2]_{R12}$ -correction, *Phys. Chem. Chem. Phys.* **24**, 13550 (2022).
- [36] I. O. Sokolov, W. Dobrautz, H. Luo, A. Alavi, and I. Tavernelli, Orders of magnitude reduction in the computational overhead for quantum many-body problems on quantum computers via an exact transcorrelated method (2022), arXiv preprint [ArXiv:2201.03049](https://arxiv.org/abs/2201.03049).
- [37] D. S. Steiger, T. Häner, and M. Troyer, ProjectQ: An open source software framework for quantum computing, *Quantum* **2**, 49 (2018).
- [38] A. Kumar, A. Asthana, C. Masteran, E. F. Valeev, Y. Zhang, L. Cincio, S. Tretiak, and P. A. Dub, Accurate quantum simulation of molecular ground and excited states with a transcorrelated Hamiltonian (2022), arXiv preprint [ArXiv:2201.09852](https://arxiv.org/abs/2201.09852).
- [39] T. Yanai and T. Shiozaki, Canonical transcorrelated theory with projected Slater-type geminals, *J. Chem. Phys.* **136**, 084107 (2012).
- [40] S. R. White, Numerical canonical transformation approach to quantum many-body problems, *J. Chem. Phys.* **117**, 7472 (2002).
- [41] T. Yanai and G. K.-L. Chan, Canonical transformation theory for multireference problems, *J. Chem. Phys.* **124**, 194106 (2006).
- [42] T. Yanai, Y. Kurashige, E. Neuscammann, and G. K.-L. Chan, Multireference quantum chemistry through a joint density matrix renormalization group and canonical transformation theory, *J. Chem. Phys.* **132**, 024105 (2010).
- [43] F. Spiegelmann and J. P. Malrieu, The use of effective Hamiltonians for the treatment of avoided crossings. I. Adiabatic potential curves, *J. Phys. B At. Mol. Phys.* **17**, 1235 (1984).
- [44] D. I. Lyakh, M. Musiał, V. F. Lotrich, and R. J. Bartlett, Multireference nature of chemistry: The coupled-cluster view, *Chem. Rev.* **112**, 182 (2012).
- [45] A. Köhn, M. Hanauer, L. A. Mück, T.-C. Jagau, and J. Gauss, State-specific multireference coupled-cluster theory, *Wiley Interdiscip. Rev.: Comput. Mol. Sci.* **3**, 176 (2013).
- [46] F. A. Evangelista, Perspective: Multireference coupled cluster theories of dynamical electron correlation, *J. Chem. Phys.* **149**, 030901 (2018).
- [47] N. P. Bauman, E. J. Bylaska, S. Krishnamoorthy, G. H. Low, N. Wiebe, C. E. Granade, M. Roetteler, M. Troyer, and K. Kowalski, Downfolding of many-body Hamiltonians using active-space models: Extension of the sub-system embedding sub-algebras approach to unitary coupled cluster formalisms, *J. Chem. Phys.* **151**, 014107 (2019).
- [48] M. Metcalf, N. P. Bauman, K. Kowalski, and W. A. de Jong, Resource-efficient chemistry on quantum computers with the variational quantum eigensolver and the double unitary coupled-cluster approach, *J. Chem. Theory Comput.* **16**, 6165 (2020).
- [49] N. P. Bauman, J. Chladek, L. Veis, J. Pittner, and K. Kowalski, Variational quantum eigensolver for approximate diagonalization of downfolded Hamiltonians using generalized unitary coupled cluster ansatz, *Quantum Sci. Technol.* **6**, 034008 (2021).
- [50] N. T. Le and L. N. Tran, Correlated reference-assisted variational quantum eigensolver (2022), e-print [ArXiv:2205.03539](https://arxiv.org/abs/2205.03539).
- [51] F. A. Evangelista, A driven similarity renormalization group approach to quantum many-body problems, *J. Chem. Phys.* **141**, 054109 (2014).
- [52] C. Li and F. A. Evangelista, Multireference driven similarity renormalization group: A second-order perturbative analysis, *J. Chem. Theory Comput.* **11**, 2097 (2015).
- [53] C. Li and F. A. Evangelista, Towards numerically robust multireference theories: The driven similarity renormalization group truncated to one- and two-body operators, *J. Chem. Phys.* **144**, 164114 (2016).
- [54] C. Li and F. A. Evangelista, Multireference theories of electron correlation based on the driven similarity renormalization group, *Annu. Rev. Phys. Chem.* **70**, 245 (2019).
- [55] F. Wegner, Flow-equations for Hamiltonians, *Ann. Phys.* **506**, 77 (1994).
- [56] S. D. Głazek and K. G. Wilson, Perturbative renormalization group for Hamiltonians, *Phys. Rev. D* **49**, 4214 (1994).
- [57] K. Tsukiyama, S. K. Bogner, and A. Schwenk, In-medium similarity renormalization group for open-shell nuclei, *Phys. Rev. C* **85**, 061304 (2012).
- [58] H. Hergert, In-medium similarity renormalization group for closed and open-shell nuclei, *Phys. Scr.* **92**, 023002 (2017).
- [59] R. M. Parrish and P. L. McMahon, Quantum filter diagonalization: Quantum eigendecomposition without full quantum phase estimation (2019), arXiv e-prints, [ArXiv:1909.08925](https://arxiv.org/abs/1909.08925).
- [60] N. H. Stair, R. Huang, and F. A. Evangelista, A multireference quantum Krylov algorithm for strongly correlated electrons, *J. Chem. Theory Comput.* **16**, 2236 (2020).
- [61] J. Cohn, M. Motta, and R. M. Parrish, Quantum Filter Diagonalization with Compressed Double-Factorized Hamiltonians, *PRX Quantum* **2**, 040352 (2021).

- [62] J. Shen and P. Piecuch, Combining active-space coupled-cluster methods with moment energy corrections via the $CC(p;q)$ methodology, with benchmark calculations for biradical transition states, *J. Chem. Phys.* **136**, 144104 (2012).
- [63] Google AI Quantum and Collaborators, Hartree-Fock on a superconducting qubit quantum computer, *Science* **369**, 1084 (2020).
- [64] M. Motta, G. O. Jones, J. E. Rice, T. P. Gujarati, R. Sakuma, I. Liepuoniute, J. M. Garcia, and Y.-y. Ohnishi, Quantum chemistry simulation of ground- and excited-state properties of the sulfonium cation on a superconducting quantum processor (2022), arXiv preprint [ArXiv:2208.02414](https://arxiv.org/abs/2208.02414).
- [65] T. E. O'Brien, G. Anselmetti, F. Gkritis, V. Elfving, S. Polla, W. J. Huggins, O. Oumarou, K. Kechedzhi, D. Abanin, and R. Acharya, *et al.*, Purification-based quantum error mitigation of pair-correlated electron simulations (2022), arXiv preprint [ArXiv:2210.10799](https://arxiv.org/abs/2210.10799).
- [66] C. Li and F. A. Evangelista, Spin-free formulation of the multireference driven similarity renormalization group: A benchmark study of first-row diatomic molecules and spin-crossover energetics, *J. Chem. Phys.* **155**, 114111 (2021).
- [67] J. D. Watts, G. W. Trucks, and R. J. Bartlett, The unitary coupled-cluster approach and molecular properties: Applications of the UCC(4) method, *Chem. Phys. Lett.* **157**, 359 (1989).
- [68] M. Musial and R. J. Bartlett, Intermediate Hamiltonian Fock-space multireference coupled-cluster method with full triples for calculation of excitation energies, *J. Chem. Phys.* **129**, 044101 (2008).
- [69] M. Musial and R. J. Bartlett, Multireference Fock-space coupled-cluster and equation-of-motion coupled-cluster theories: The detailed interconnections, *J. Chem. Phys.* **129**, 134105 (2008).
- [70] T. D. Crawford and H. F. Schaefer, An introduction to coupled cluster theory for computational chemists, *Rev. Comp. Chem.* **14**, 33 (2000).
- [71] D. Mukherjee, Normal ordering and a Wick-like reduction theorem for fermions with respect to a multi-determinantal reference state, *Chem. Phys. Lett.* **274**, 561 (1997).
- [72] W. Kutzelnigg and D. Mukherjee, Normal order and extended Wick theorem for a multiconfiguration reference wave function, *J. Chem. Phys.* **107**, 432 (1997).
- [73] F. A. Evangelista and J. Gauss, On the approximation of the similarity-transformed Hamiltonian in single-reference and multireference coupled cluster theory, *Chem. Phys.* **401**, 27 (2012).
- [74] E. Neuscamman, T. Yanai, and G. K.-L. Chan, Quadratic canonical transformation theory and higher order density matrices, *J. Chem. Phys.* **130**, 124102 (2009).
- [75] C. Li and F. A. Evangelista, Connected three-body terms in single-reference unitary many-body theories: Iterative and perturbative approximations, *J. Chem. Phys.* **152**, 234116 (2020).
- [76] K. Andersson, P.-Å. Malmqvist, and B. O. Roos, Second-order perturbation theory with a complete active space self-consistent field reference function, *J. Chem. Phys.* **96**, 1218 (1992).
- [77] W. Kutzelnigg, Quantum chemistry in Fock space. I. The universal wave and energy operators, *J. Chem. Phys.* **77**, 3081 (1982).
- [78] D. A. Mazziotti, Contracted Schrödinger equation: Determining quantum energies and two-particle density matrices without wave functions, *Phys. Rev. A* **57**, 4219 (1998).
- [79] W. Kutzelnigg and D. Mukherjee, Cumulant expansion of the reduced density matrices, *J. Chem. Phys.* **110**, 2800 (1999).
- [80] S. Wang, C. Li, and F. A. Evangelista, Analytic energy gradients for the driven similarity renormalization group multireference second-order perturbation theory, *J. Chem. Theory Comput.* **17**, 7666 (2021).
- [81] N. He, C. Li, and F. A. Evangelista, Second-order active-space embedding theory, *J. Chem. Theory Comput.* **18**, 1527 (2022).
- [82] A. Zhao, N. C. Rubin, and A. Miyake, Fermionic Partial Tomography via Classical Shadows, *Phys. Rev. Lett.* **127**, 110504 (2021).
- [83] F. A. Evangelista, FORTE: A suite of quantum chemistry methods for strongly correlated electrons (2021).
- [84] D. G. A. Smith, *et al.*, PS14 1.4: Open-source software for high-throughput quantum chemistry, *J. Chem. Phys.* **152**, 184108 (2020).
- [85] T. H. Dunning, Gaussian basis sets for use in correlated molecular calculations. I. The atoms boron through neon and hydrogen, *J. Chem. Phys.* **90**, 1007 (1989).
- [86] F. Colmenero, C. Pérez del Valle, and C. Valdemoro, Approximating q -order reduced density matrices in terms of the lower-order ones. I. General relations., *Phys. Rev. A* **47**, 971 (1993).
- [87] A. E. DePrince and D. A. Mazziotti, Cumulant reconstruction of the three-electron reduced density matrix in the anti-Hermitian contracted Schrödinger equation, *J. Chem. Phys.* **127**, 104104 (2007).
- [88] M. L. Abrams and C. D. Sherrill, Natural orbitals as substitutes for optimized orbitals in complete active space wavefunctions, *Chem. Phys. Lett.* **395**, 227 (2004).
- [89] J. Romero, R. Babbush, J. R. McClean, C. Hempel, P. J. Love, and A. Aspuru-Guzik, Strategies for quantum computing molecular energies using the unitary coupled cluster ansatz, *Quantum Sci. Technol.* **4**, 014008 (2019).
- [90] C. Garrod and J. K. Percus, Reduction of the n -particle variational problem, *J. Math. Phys.* **5**, 1756 (1964).
- [91] R. M. Erdahl, Representability, *Int. J. Quantum Chem.* **13**, 697 (1978).
- [92] Z. Zhao, B. J. Braams, M. Fukuda, M. L. Overton, and J. K. Percus, The reduced density matrix method for electronic structure calculations and the role of three-index representability conditions, *J. Comp. Phys.* **120**, 2095 (2004).
- [93] D. A. Mazziotti, Structure of Fermionic Density Matrices: Complete n -Representability Conditions, *Phys. Rev. Lett.* **108**, 263002 (2012).
- [94] N. C. Rubin, R. Babbush, and J. McClean, Application of fermionic marginal constraints to hybrid quantum algorithms, *New J. Phys.* **20**, 053020 (2018).
- [95] A. Leszczyk, M. Máté, O. Legeza, and K. Boguslawski, Assessing the accuracy of tailored coupled cluster

- methods corrected by electronic wave functions of polynomial cost, *J. Chem. Theory Comput.* **18**, 96 (2021).
- [96] C. Li and F. A. Evangelista, Towards numerically robust multireference theories: The driven similarity renormalization group truncated to one- and two-body operators, *J. Chem. Phys.* **144**, 164114 (2016).
- [97] I. Shavitt and R. J. Bartlett, *Many-Body Methods in Chemistry and Physics: MBPT and Coupled-Cluster Theory* (Cambridge University Press, Cambridge, England, 2009).
- [98] K. Raghavachari, G. W. Trucks, J. A. Pople, and M. Head-Gordon, A fifth-order perturbation comparison of electron correlation theories, *Chem. Phys. Lett.* **157**, 479 (1989).
- [99] S. R. White, Density Matrix Formulation for Quantum Renormalization Groups, *Phys. Rev. Lett.* **69**, 2863 (1992).
- [100] H.-J. Werner and P. J. Knowles, An efficient internally contracted multiconfiguration reference configuration-interaction method, *J. Chem. Phys.* **89**, 5803 (1988).
- [101] P. J. Knowles and H.-J. Werner, An efficient method for the evaluation of coupling-coefficients in configuration-interaction calculations, *Chem. Phys. Lett.* **145**, 514 (1988).
- [102] S. R. Langhoff and E. R. Davidson, Configuration interaction calculations on the nitrogen molecule, *Int. J. Quantum Chem.* **8**, 61 (1974).
- [103] F. A. Evangelista, W. D. Allen, and H. F. Schaefer, Coupling term derivation and general implementation of state-specific multireference coupled cluster theories, *J. Chem. Phys.* **127**, 024102 (2007).
- [104] F. A. Evangelista, M. Hanauer, A. Koehn, and J. Gauss, A sequential transformation approach to the internally contracted multireference coupled cluster method, *J. Chem. Phys.* **136**, 204108 (2012).
- [105] P. Wenthold, R. Squires, and W. Lineberger, Ultraviolet photoelectron spectroscopy of the *o*-, *m*-, and *p*-benzynes negative ions: Electron affinities and singlet-triplet splittings for *o*-, *m*-, and *p*-benzyne, *J. Am. Chem. Soc.* **120**, 5279 (1998).
- [106] M. Hanauer and A. Köhn, Perturbative treatment of triple excitations in internally contracted multireference coupled cluster theory, *J. Chem. Phys.* **136**, 204107 (2012).
- [107] A. Perera, R. W. Molt, V. F. Lotrich, and R. J. Bartlett, Singlet-triplet separations of di-radicals treated by the DEA/DIP-EOM-CCSD methods, *Theor. Chem. Acc.* **133**, 1514 (2014).
- [108] S. Gulania, E. F. Kjørnstad, J. F. Stanton, H. Koch, and A. I. Krylov, Equation-of-motion coupled-cluster method with double electron-attaching operators: Theory, implementation, and benchmarks, *J. Chem. Phys.* **154**, 114115 (2021).
- [109] P. U. Manohar and A. I. Krylov, A noniterative perturbative triples correction for the spin-flipping and spin-conserving equation-of-motion coupled-cluster methods with single and double substitutions, *J. Chem. Phys.* **129**, 194105 (2008).
- [110] L. Slipchenko and A. I. Krylov, Singlet-triplet gaps in diradicals by the spin-flip approach: A benchmark study, *J. Chem. Phys.* **117**, 4694 (2002).
- [111] X. Li and J. Paldus, Electronic structure of organic diradicals: Evaluation of the performance of coupled-cluster methods, *J. Chem. Phys.* **129**, 174101 (2008).
- [112] C. J. Cramer, J. Nash, and R. Squires, A reinvestigation of singlet benzyne thermochemistry predicted by CASPT2, coupled-cluster and density functional calculations, *Chem. Phys. Lett.* **277**, 311 (1997).
- [113] R. Lindh, A. Bernhardsson, and M. Schütz, Benzyne thermochemistry: A benchmark ab initio study, *J. Phys. Chem. A* **103**, 9913 (1999).
- [114] H. Li, S.-Y. Yu, M.-B. Huang, and Z.-X. Wang, The S_1 states of *o*-, *m*-, and *p*-benzyne studied using multiconfiguration second-order perturbation theory, *Chem. Phys. Lett.* **450**, 12 (2007).
- [115] E. B. Wang, C. A. Parish, and H. Lischka, An extended multireference study of the electronic states of *para*-benzyne, *J. Chem. Phys.* **129**, 044306 (2008).
- [116] S. Wang, C. Li, and F. A. Evangelista, Analytic gradients for the single-reference driven similarity renormalization group second-order perturbation theory, *J. Chem. Phys.* **151**, 044118 (2019).
- [117] G. Aleksandrowicz *et al.*, Qiskit: An Open-source Framework for Quantum Computing (2021).
- [118] A. Kinal and P. Piecuch, Computational investigation of the conrotatory and disrotatory isomerization channels of bicyclo [1.1. 0] butane to buta-1, 3-diene: A completely renormalized coupled-cluster study, *J. Phys. Chem. A* **111**, 734 (2007).
- [119] R. Berner and A. Lüchow, Isomerization of bicyclo [1.1. 0] butane by means of the diffusion quantum Monte Carlo method, *J. Phys. Chem. A* **114**, 13222 (2010).
- [120] R. Srinivasan, A. Levi, and I. Haller, The thermal decomposition of bicyclo [1.1. 0] butane, *J. Phys. Chem.* **69**, 1775 (1965).
- [121] K. B. Wiberg and R. A. Fenoglio, Heats of formation of C_4H_6 hydrocarbons, *J. Am. Chem. Soc.* **90**, 3395 (1968).
- [122] E. Blanchard Jr and A. Cairncross, Bicyclo[1.1.0]butane chemistry. I. The synthesis and reactions of 3-methylbicyclo[1.1.0]butanecarbonitriles, *J. Am. Chem. Soc.* **88**, 487 (1966).
- [123] H. Frey and I. Stevens, Thermal unimolecular isomerization of bicyclobutane, *Trans. Faraday Soc.* **61**, 90 (1965).
- [124] K. B. Wiberg and J. M. Lavanish, Formation and thermal decomposition of bicyclo[1.1.0]butane-2-exo- d_1^1 , *J. Am. Chem. Soc.* **88**, 5272 (1966).
- [125] G. Closs and P. Pfeffer, The steric course of the thermal rearrangements of methylbicyclobutanes, *J. Am. Chem. Soc.* **90**, 2452 (1968).
- [126] D. A. Mazziotti, Energy barriers in the conversion of bicyclobutane to gauche-1, 3-butadiene from the anti-Hermitian contracted Schrödinger equation, *J. Phys. Chem. A* **112**, 13684 (2008).
- [127] K. A. Nguyen and M. S. Gordon, Isomerization of bicyclo [1.1. 0] butane to butadiene, *J. Am. Chem. Soc.* **117**, 3835 (1995).
- [128] J. J. Lutz and P. Piecuch, Extrapolating potential energy surfaces by scaling electron correlation: Isomerization of

- bicyclobutane to butadiene, *J. Chem. Phys.* **128**, 154116 (2008).
- [129] J.-N. Boyn and D. A. Mazziotti, Elucidating the molecular orbital dependence of the total electronic energy in multireference problems, *J. Chem. Phys.* **156**, 194104 (2022).
- [130] J. F. Gonthier, M. D. Radin, C. Buda, E. J. Duskocil, C. M. Abuan, and J. Romero, Measurements as a roadblock to near-term practical quantum advantage in chemistry: Resource analysis, *Phys. Rev. Res.* **4**, 033154 (2022).
- [131] W. D. Allen and H. F. Schaefer, *Ab initio* studies of the low-lying electronic states of ketene, *J. Chem. Phys.* **84**, 2212 (1986).
- [132] W. D. Allen and H. F. Schaefer, An examination of the 2^1A_1 states of formaldehyde and ketene including analytic configuration interaction energy first derivatives for singlet excited electronic states of the same symmetry as the ground state, *J. Chem. Phys.* **87**, 7076 (1987).
- [133] R. M. Parrish, J. T. Iosue, A. Ozaeta, and P. L. McMahon, A Jacobi diagonalization and Anderson acceleration algorithm for variational quantum algorithm parameter optimization (2019), arXiv preprint [ArXiv:1904.03206](https://arxiv.org/abs/1904.03206).
- [134] K. M. Nakanishi, K. Fujii, and S. Todo, Sequential minimal optimization for quantum-classical hybrid algorithms, *Phys. Rev. Res.* **2**, 043158 (2020).